GENETICS

ATM and 53BP1 regulate alternative end joining–mediated V(D)J recombination

Jinglong Wang*, Cheyenne A. Sadeghi, Long V. Le, Marie Le Bouteiller, Richard L. Frock*

G_0-G_1 phase alternative end joining (A-EJ) is a recently defined mutagenic pathway characterized by resected deletion and translocation joints that are predominantly direct and are distinguished from A-EJ in cycling cells that rely much more on microhomology-mediated end joining (MMEJ). Using chemical and genetic approaches, we systematically evaluate potential A-EJ factors and DNA damage response (DDR) genes to support this mechanism by mapping the repair fates of RAG1/2-initiated double-strand breaks in the context of Igκ locus V-J recombination and chromosome translocation. Our findings highlight a polymerase theta–independent Parp1-XRCC1/LigIII axis as central A-EJ components, supported by 53BP1 in the context of an Ataxia-telangiectasia mutated (ATM)–activated DDR. Mechanistically, we demonstrate varied changes in short-range resection, MMEJ, and translocation, imposed by compromising specific DDR activities, which include polymerase alpha, Ataxia-telangiectasia and Rad3-related (ATR), DNA2, and Mre11. This study advances our understanding of DNA damage repair within the 53BP1 regulatory domain and the RAG1/2 postcleavage complex.

INTRODUCTION

V(D)J recombination assembles the variable region of antigen receptor loci in the G_0-G_1 phase of the cell cycle and is essential for B and T cell development. Recombination is highly coordinated, involving the loading of the RAG1/2 endonuclease at J region recombination centers, pairing of D or V gene segments across chromatin loops, RAG1/2 incision, hairpin opening and processing of the coding ends, ligation of coding ends, and, separately, ligation of blunt recombination sequence (signal) ends (*1*, *2*). The primary mechanism for ligation is nonhomologous end joining (NHEJ). However, core NHEJ deficiency [i.e., Ku70, Ku80, XRCC4, or DNA Ligase IV (Lig4)] reveals an alternative end joining (A-EJ) machinery that completes DNA double-strand break (DSB) repair to varying degrees. For instance, while A-EJ in the absence of XRCC4 or LigIV deficiency is extremely low in the G_0-G_1 phase, it is quite robust in cycling phases, characterized by kilobase-long resection and near-exclusive junctional microhomology (MH) utilization (*3*, *4*). In contrast, G_0-G_1 A-EJ in the absence of Ku70 is robust, though less efficient than NHEJ, repairing both Cas9 and RAG1/2 DSBs with a limited resection window and a greater direct to MH ratio that more closely resembles NHEJ than *Lig4*$^{-/-}$ (*4*). However, a key discerning feature for V(D)J recombination by either A-EJ mechanism is the loss in biased joining of coding ends to each other and likewise for signal ends. Thus, end joining in the absence of Ku70/80 represents a true A-EJ mechanism, whereas the absence of XRCC4/LigIV represents an end-joining mechanism influenced by NHEJ intermediates (*4*).

Despite its significance in tumorigenesis (*5*), A-EJ mechanisms remain poorly understood. Early identified components in cycling cells included Parp1, XRCC1, and LigIII (*6*, *7*), which contribute to chromosome translocation in mouse embryonic stem cells. In this context, LigI acts as a backup ligase for A-EJ (*8*) but is redundant for IgH class switch recombination (*9*, *10*). A more recently identified A-EJ component, Polθ, operates on DNA ends in the absence of Ku70/Ku80 (*11*, *12*) and functions independently of Parp1 when repairing G_0-G_1 DSBs in the S-G_2-M phase (*3*). Therefore, it remains unclear which A-EJ mechanisms operate in the G_0-G_1 phase given junction structure and repair capacity differences between noncycling and cycling cells (*4*).

Microhomology-mediated end joining (MMEJ) is not exclusive to a single pathway but rather indicates the extent to which end hybridization is necessary to complete repair [typically 2 to 20 base pairs (bp)]. Junctional MHs formed by A-EJ involve limited resection and fill-in processes. Implicated factors include, among others, CtIP (*13*), Mre11 and associated RAD50-NBS1 (MRN) (*14*–*17*), and loaders of DNA clamps to tether polymerases, such as polymerase theta (Polθ) and polymerase lambda (Polλ) (*11*, *18*–*22*). Ataxia-telangiectasia mutated (ATM)–mediated phosphorylation of CtIP stimulates sequential Mre11 endo- and exonuclease activity to remove protein-bound or -adducted 5′ ends (*23*–*26*), whereas DNA2 promotes resection of clean ends (*27*). CtIP also promotes DNA2-dependent long-range resection that is separate from an Exo1-dependent mechanism (*28*–*30*).

A central regulator of resection that is associated with the full establishment of the DNA damage response (DDR) is 53BP1, which recruits multiple complexes [i.e., Shieldin, CST-Polα, Dynll1 dimers, TOPBP1 with Ataxia-telangiectasia and Rad3-related (ATR), and PTIP] to regulate DNA end resection (*31*–*38*). Although 53BP1 generally supports NHEJ, it is unclear how these associated complexes support NHEJ. This is further complicated with A-EJ mechanisms that generate resected intermediates to complete repair. Notably, Exo1 is the primary nuclease responsible for long-range resection in G_0-G_1 phase LigIV-deficient cells, and both Exo1 and DNA2 contribute to long-range resection in cells that are additionally deficient in 53BP1 (*39*). In this context, long range resection in LigIV/53BP1 double-deficient cells is mediated by ATM (*40*), which also initiates the DDR with DNA-PKcs, as a functional kinase with Ku70/Ku80, to stabilize end synapsis. While it is clear that DSB-associated resection in the G_0-G_1 phase occurs in the absence of core NHEJ factors (*4*, *39*), it is unknown how the DDR regulates A-EJ mechanisms in this context.

Here, we identify the Parp1-XRCC1-LigIII axis as the primary driver of A-EJ–mediated Igκ locus V(D)J recombination in the absence of Ku70. Inhibited V-J recombination due to DDR or candidate

Division of Radiation and Cancer Biology, Department of Radiation Oncology, Stanford University School of Medicine, Stanford, CA 94305, USA.
*Corresponding author. Email: frock@stanford.edu (R.L.F.); jlwang90@stanford.edu (J.W.)

repair factor perturbation is accompanied by joints with increased resection and an increased MH over direct joint utilization where ATR, Mre11 exonuclease, polymerase alpha and DNA2 inhibition affect these measures to varying degrees. In this regard, MMEJ utilization becomes near exclusive in *Ku70*$^{-/-}$*Xrcc1*$^{-/-}$ cells and in *Ku70*$^{-/-}$*Parp1*$^{-/-}$ cells synergized with ATM inhibition. Crucially, we also find that A-EJ repair capacity is reliant on 53BP1 in the context of the ATM-initiated DDR. ATM and Parp1 separately support the residual recombination fidelity of coding ends by A-EJ. ATM also suppresses excessive distal V-J recombination and interchromosomal translocations, predominantly to other RAG1/2 DSBs. Other inhibited DDR genes also increase translocations at the cost of V-J recombination efficiency and contrasts that of XRCC1 or 53BP1 deficiencies that are uniformly end joining defective.

RESULTS

To elucidate mechanistic factors for Ku-independent A-EJ and their regulation, we knocked out several DDR or candidate A-EJ genes in the *Ku70*$^{-/-}$, *Ku70*$^{-/-}$*53bp1*$^{-/-}$, and *Lig4*$^{-/-}$*Ku70*$^{-/-}$ Abelson kinase transformed murine progenitor B (*vAbl*) cell lines and validated low levels of prior endogenous V(D)J recombination (fig. S1, A to J, and tables S1 to S4). Ku70 was complemented to restore NHEJ and contrast A-EJ phenotypes. We used a panel of common inhibitors of implicated kinases, polymerases, and nucleases in both wild-type (WT) and *Ku70*$^{-/-}$ backgrounds to determine the core A-EJ pathway and its regulators (see Materials and Methods for cited doses). *vAbl* cells were assayed for physiologic V(D)J recombination under G_0-G_1 arrest by the Abl kinase inhibitor STI-571 (*4*, *40*, *41*, *42*) and for cell viability to optimize compound efficacy and interpretation of recombined junctions. Overall, most inhibitors exhibited minimal effects, though Polα inhibition had a discernible impact on cell viability (fig. S2, A to L).

We measured Igκ locus V-J recombination and interchromosomal translocations by A-EJ in *Ku70*$^{-/-}$ and derivative *vAbl* cells using the high-throughput rejoin and genome-wide translocation sequencing platform, *HTGTS-JoinT-seq* (*4*, *43*), from the Jκ1 bait DSB position (fig. S3A). We used baits from each side of the DSB corresponding to both the hairpin sealed coding end (Jκ1CE) and blunt signal end (Jκ1SE), a result of paired RAG1/2 DSB cleavage in complex with one of 100+ corresponding Vκ coding/signal end preys. This locus also contains Vκ gene segments organized in deletional (DEL) or inversional (INV) strand orientations with respect to the Jκ region that can result in a variety of deletions, inversions, and excision circles when viewed from the coding or signal ends of the Jκ1 bait DSB (Fig. 1A and figs. S3A and S4A). In general, although chemical or genetic perturbation of A-EJ yielded similar results for both bait ends, with some exceptions highlighted below, signal ends tended to recover more junctions than coding end baits. The same outcome did not occur for NHEJ, indicating that hairpin opening, an end processing event that is required for accessibility and subsequent ligation of coding ends, may be rate limiting.

XRCC1, Parp1, and DDR components support A-EJ of Igκ locus DSBs

As A-EJ recombines Vκ-Jκ regions with significantly less bias (i.e., CE-CE and SE-SE) than NHEJ (*4*), we incorporated repair to both CEs and SEs in the Vκ region, normalized against the total sequence reads, which include other repair outcomes (e.g., rejoined or recombined Jκ DSBs and translocations), to derive the V-J recombination efficiency (V-J Eff) (Fig. 1A and fig. S4A) (see Materials and Methods). Using this approach, we separated analysis of gene perturbations in the *Ku70*$^{-/-}$ parental background into two distinct groups: putative core factors (Parp1, Polθ, and XRCC1) and DDR factors involved in regulation (ATM and ATR) or DNA end processing (Polα, Mre11, and DNA2).

Regarding putative core factors, we found that inhibition of multiple Parp genes (Parpi #1/2) or deletion of Parp1 (*Parp1*$^{-/-}$ #1/2) decreased V-J efficiency by 80 and 30% for the CE bait and 85 and 80% for the SE bait, respectively (Fig. 1, A to C; figs. S3B and S4, B and D; and tables S3 and S4), indicating that Parp genes play a significant role in this process. We next wanted to know whether Polθ participates in this mechanism despite its very poor expression in the G_0-G_1 phase (*3*). Here, Polθi #2 had no impact on V-J recombination efficiency (Fig. 1B and fig. S4C); however, Polθi #1 decreased both WT and *Ku70*$^{-/-}$ recombination (Fig. 1B and figs. S4C and S5, B and C). Given that Polθi #1 (Novobiocin) also affects adenosine triphosphatase (ATPase) activities of multiple classes of proteins (*44*), some of which may be important for recombination, whereas Polθi #2 (ART558) is, to date, more extensively characterized (*45*), we propose that Polθ plays a minimal role at best in Ku-independent V(D)J recombination. We next determined which A-EJ components drive ligation. As nuclear LigIII activity depends on XRCC1 (*9*, *46*), and likewise for LigI with PCNA (*47*), we compared total protein levels of the A-EJ ligases in cycling versus G_0-G_1 arrest. LigIII abundance was only slightly decreased (Fig. 1D), whereas LigI levels plummeted fivefold by day 2, when cells are arrested, and was nearly absent by day 4 (Fig. 1E). This suggests that LigIII is the primary A-EJ ligase in this G_0-G_1 setting. As predicted from cycling cells (*48*), XRCC1 deletion reduced steady-state protein levels of LigIII by sixfold but did not affect LigI (Fig. 1, D and E), indicating that XRCC1 specifically stabilizes LigIII protein levels. In this regard, XRCC1 deletion essentially abolished V-J recombination, resulting in a robust one to two orders of magnitude decrease (Fig. 1C and figs. S3B and S4, B and D), revealing a core A-EJ role for XRCC1/LigIII. Collectively, the data support a Parp1-XRCC1-LigIII axis driving G_0-G_1 phase A-EJ.

With regard to the regulation of A-EJ, both ATR and ATM inhibition displayed modest reductions (~40 to 50%) in V-J recombination (Fig. 1, B and C, and figs. S3B and S4, B and C), indicating that DDR kinase activities partially facilitate A-EJ. Although ATMi treatment of *Ku70*$^{-/-}$*Atm*$^{-/-}$ *vAbl* cells had no additional impact on V-J efficiency (Fig. 1C and fig. S4C), deletion of ATM in *Ku70*$^{-/-}$ cells did not decrease V-J efficiency as it did with ATMi alone. This suggests that a dominant negative activity suppresses overlapping DDR kinase functions. As expected, NHEJ restoration via Ku70 expression in double-knockout cell lines markedly increased V-J efficiency, reaching levels twofold higher than *Ku70*$^{-/-}$ alone (Fig. 1C and fig. S4C). Inhibiting the nuclease activity of DNA2 displayed opposing efficiency changes that were dependent on the bait end. Specifically, DNA2i decreased efficiency, on par with ATRi for the SE bait, but increased efficiency by ~33% for the CE bait, which was the greatest increase of all combinations tested. This increase with DNA2i suggests competition with another factor that opens hairpins. Inhibited Mre11 nuclease activities had a smaller impact on recombination efficiency, where inhibited exonuclease activity [Mre11(ex)i] modestly increased CE bait V-J efficiency, like DNA2i, but did not affect the SE bait, unlike DNA2i (Fig. 1B and fig. S4C).

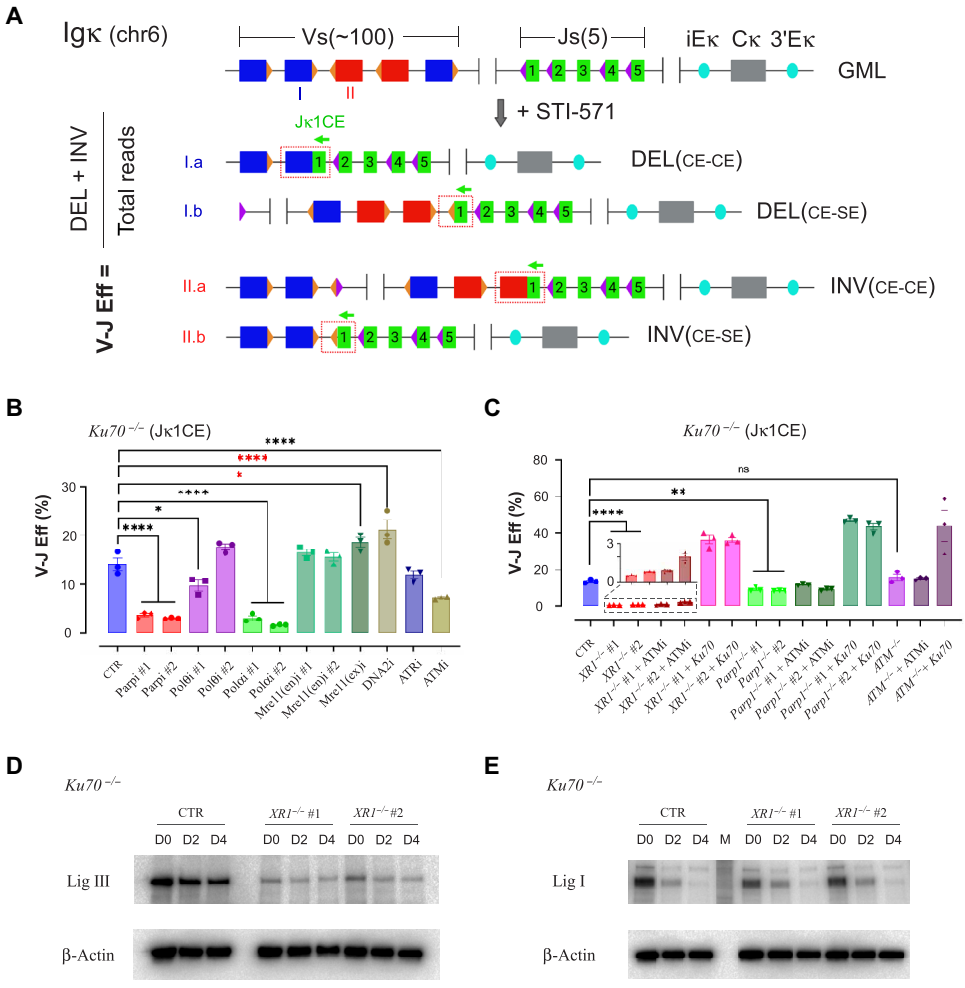

Fig. 1. XRCC1, Parp1, and DDR components support A-EJ of Igκ locus DSBs. (**A**) The murine Igκ antigen receptor locus in a germline configuration (GML), each with an associated recombination signal sequence (triangles). STI-571 treatment enables *vAbl* cells to undergo G_0-G_1 arrest and initiate V-J recombination. V gene segments are oriented in a deletion (DEL, blue; example: I) or inversion (INV, red; example: II) configuration with respect to the Jκ1 coding end (CE) bait (green arrow). The Jκ1CE can form Vκ coding (CE-CE; I.a or II.a) or hybrid (CE-SE; I.b or II.b) joints with the associated recombination signal end (SE; orange triangles). Recombination efficiency (V-J Eff) was calculated by the sum of DEL and INV V-J joints divided by the total reads. (**B**) V-J recombination efficiency of $Ku70^{-/-}$ cells with or without inhibitors. (**C**) V-J recombination efficiency changes of $Ku70^{-/-}$ *vAbl* cells with added deletions and optionally with ATMi treatment or Ku70 ectopic expression. All experiments were biologically repeated three times, and significance was determined by one-way ANOVA with posttest comparison: $*P < 0.05$, $**P < 0.01$, $****P < 0.0001$, and ns, no significance; red asterisks indicate significant increases. (**D**) Western blot of LigIII expression levels in *vAbl* $Ku70^{-/-}$ (CTR) and $Ku70^{-/-}$ $XRCC1^{-/-}$ ($XR1^{-/-}$ #1/2) cells treated by STI-571 for 0, 2, and 4 days (D0, D2, and D4), respectively, where β-actin was used as controls. (**E**) Same as (D) but for LigI expression levels.

Mre11 endonuclease inhibitors [Mre11(en)i #1/2] had no significant impact on any analysis parameter in this study. These results are in support of a prior in vitro finding that DNA2, rather than Mre11, acts as the primary nuclease for accessible ends (*27*).

To uncover additional insight into the chemical inhibitory effects specific to A-EJ, we also tested the same compounds in *WT vAbl* cells. Parpi #1/2, ATRi, and ATMi compounds also reduced V-J efficiency from both CE and SE baits (fig. S5, A to C), but the severity was attenuated compared to $Ku70^{-/-}$ cells (Fig. 1B and fig. S4C). Polα inhibition (Polαi #1/2) displayed a two- to threefold reduced V-J efficiency in both WT and $Ku70^{-/-}$ *vAbl* lines; however, the decreased viability (fig. S2, A to C, G to I) limits interpretation of junction yields, but distinguishing repair patterns are evident and described below. Overall, the data suggest that an ATM/ATR DDR mechanism supports A-EJ.

53BP1 is essential for G_0-G_1 A-EJ

We next addressed the extent to which the DDR supports A-EJ by deleting a core regulator of resection: 53BP1. Loss of 53BP1 ($Ku70^{-/-}53bp1^{-/-}$ #1/2) inhibited A-EJ, resulting in a robust decrease (10-fold for CE bait; 5-fold for SE bait) in V-J efficiency for all combinations (Fig. 2, A and B; figs. S6, A and B, and S7, A to C; tables S3 and S4) but was still comparably higher than $Ku70^{-/-}Xrcc1^{-/-}$ (#1/2) cells across experiments. As Exo1 is a crucial nuclease responsible for long-range resection in *vAbl* cells without 53BP1 (*39*), we generated $Ku70^{-/-}53bp1^{-/-}Exo1^{-/-}$ (#1/2/3) cells to determine whether recombination efficiency was restored. Unexpectedly, no marked improvement was detected (fig. S6, A and B), suggesting something beyond hyper-resection control is necessary to restore V-J efficiency. Similarly, Exo1 deletion in $Ku70^{-/-}$ cells did not alter the recombination efficiency

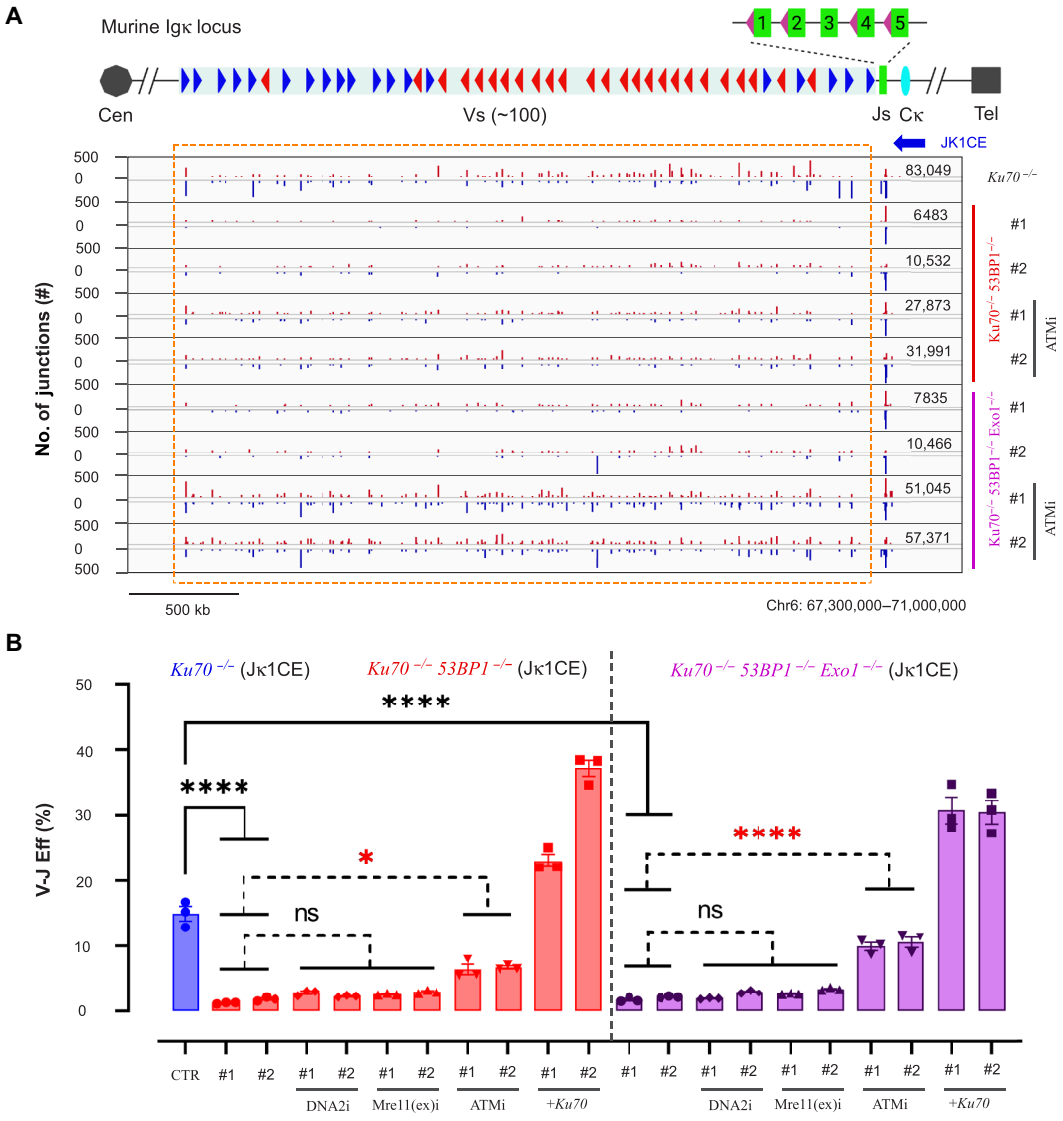

Fig. 2. 53BP1 is essential for G_0-G_1 A-EJ. (**A**) Representative *Ku70*$^{-/-}$ CE bait junction plots as described in fig. S3B but in the context of 53BP1 single or 53BP1/Exo1 double deletion, with or without ATM inhibition. (**B**) V-J recombination of the above backgrounds, with or without DNA2, Mre11(ex), and ATM inhibitors, or Ku70 rescue expression. Differences within *Ku70*$^{-/-}$*53BP1*$^{-/-}$ (red bars) and *Ku70*$^{-/-}$*53BP1*$^{-/-}$*Exo1*$^{-/-}$ (magenta bars) are evaluated by two-way ANOVA plus posttest comparison: *$P < 0.05$, ****$P < 0.0001$; black asterisks indicate significant decreases. All experiments were biologically repeated three times. (A) generated from the Integrative Genomics Viewer (igv.org).

(fig. S8, A and B), and DNA2i or Mre11(ex)i treatments to *Ku70*$^{-/-}$*53bp1*$^{-/-}$ (#1/2) and *Ku70*$^{-/-}$*53bp1*$^{-/-}$*Exo1*$^{-/-}$ cells (#1/2) also did not significantly change recombination efficiencies (fig. S6B). Therefore, we conclude Exo1 deficiency alone or in combination with inhibited DNA2 or Mre11 exonuclease activities cannot restore A-EJ-mediated V-J recombination efficiency in the absence of 53BP1.

ATM inhibition in G_0-G_1–arrested *Lig4*$^{-/-}$*53bp1*$^{-/-}$ *vAbl* cells blocks long-range resection (*40*). Therefore, we tested ATMi effects in *Ku70*$^{-/-}$*53bp1*$^{-/-}$ (#1/2) and *Ku70*$^{-/-}$*53bp1*$^{-/-}$*Exo1*$^{-/-}$ (#1/2) cells and found that V-J efficiency from CE and SE baits was restored to ~50 and ~80% of that in *Ku70*$^{-/-}$, respectively, but comparable to ATMi-treated *Ku70*$^{-/-}$ (Fig. 2, A and B, and fig. S6, A and B). Correspondingly, ATMi decreased V-J efficiency in *Ku70*$^{-/-}$*Exo1*$^{-/-}$ and *Lig4*$^{-/-}$*Ku70*$^{-/-}$ cells (figs. S7, B and C, and S8, A and B). Together, the data indicate that ATM inhibition, which partially disrupts A-EJ, can normalize the impact of 53BP1 deficiency on A-EJ. Restoring DNA-PK functionality via Ku70 complementation irrespective of 53BP1 status enhanced recombination efficiency beyond *Ku70*$^{-/-}$ except in LigIV-deficient backgrounds, which remained unchanged (*4*, *49*) (Fig. 2B; figs. S6B, S7, B and C, S8, A and B; and tables S3 and S4). In sum, we conclude that 53BP1 robustly supports A-EJ–mediated recombination in the context of the ATM-activated DDR.

A-EJ regulators and drivers, but not 53BP1, suppress resected end joining

An increased range of resected joints relative to NHEJ-mediated joints (*4*) serves as a distinguishing feature of A-EJ, which is kinetically relevant to their inherent repair efficiencies. Thus, we wanted

to know which of the above perturbations affected resected joint distributions. To do this, Vκ joints were pooled and remapped to an absolute DSB position located between the prey coding end and its adjacent signal end for both Jκ1CE and Jκ1SE baits. In *WT vAbl* cells, SE baits were joined to SE preys, likewise for CE baits/preys, and were exclusive to a ±10-bp window around the Vκ DSB sites (fig. S9, A to C). In contrast, *Ku70*$^{-/-}$ CE and SE baits each contained a mix of CE and SE prey joints with distributions that extended far beyond this window (Fig. 3A and fig. S10, A to D). Therefore, we derived the fraction enriched within the ±10-bp DSB window to discern changes in resected joint distributions. Despite varied effects on V-J efficiencies with the inhibitor panel in WT cells (fig. S5, B and C), none of them promoted resected end joining (fig. S9, B and C). In contrast, Parp (#1/2), Polα (#1/2), and ATM inhibitors increased the fraction of resected joints in *Ku70*$^{-/-}$ cells (Fig. 3, A and B, and fig. S10, A and B). *Parp1*$^{-/-}$ (#1/2), *Atm*$^{-/-}$, or *Xrcc1*$^{-/-}$ (#1/2) in *Ku70*$^{-/-}$ cells also significantly increased resected joints (Fig. 3C and fig. S10C). However, corresponding 53BP1, LigIV, and/or Exo1 deletions in *Ku70*$^{-/-}$ cells did not increase the resected joint fraction unless they were additionally treated with ATMi (Fig. 3D and figs. S10D and S11, A to F). In contrast, ATMi did not change joint distributions when added to *Ku70*$^{-/-}$*Parp1*$^{-/-}$ (#1/2) or *Ku70*$^{-/-}$*Xrcc1*$^{-/-}$ (#1/2) *vAbl* cells (Fig. 3C and fig. S10C). This suggests that Parp1 and XRCC1 have overlapping roles with ATM to regulate end processing. Neither DNA2 or Mre11 nuclease inhibition nor Exo1 deletion displayed an anti-resected joint enrichment in the various backgrounds (Fig. 3, A, B, and D, and figs. S9, B and C, S10, B and D, and S11, C to F), except for DNA2i in *Ku70*$^{-/-}$ cells

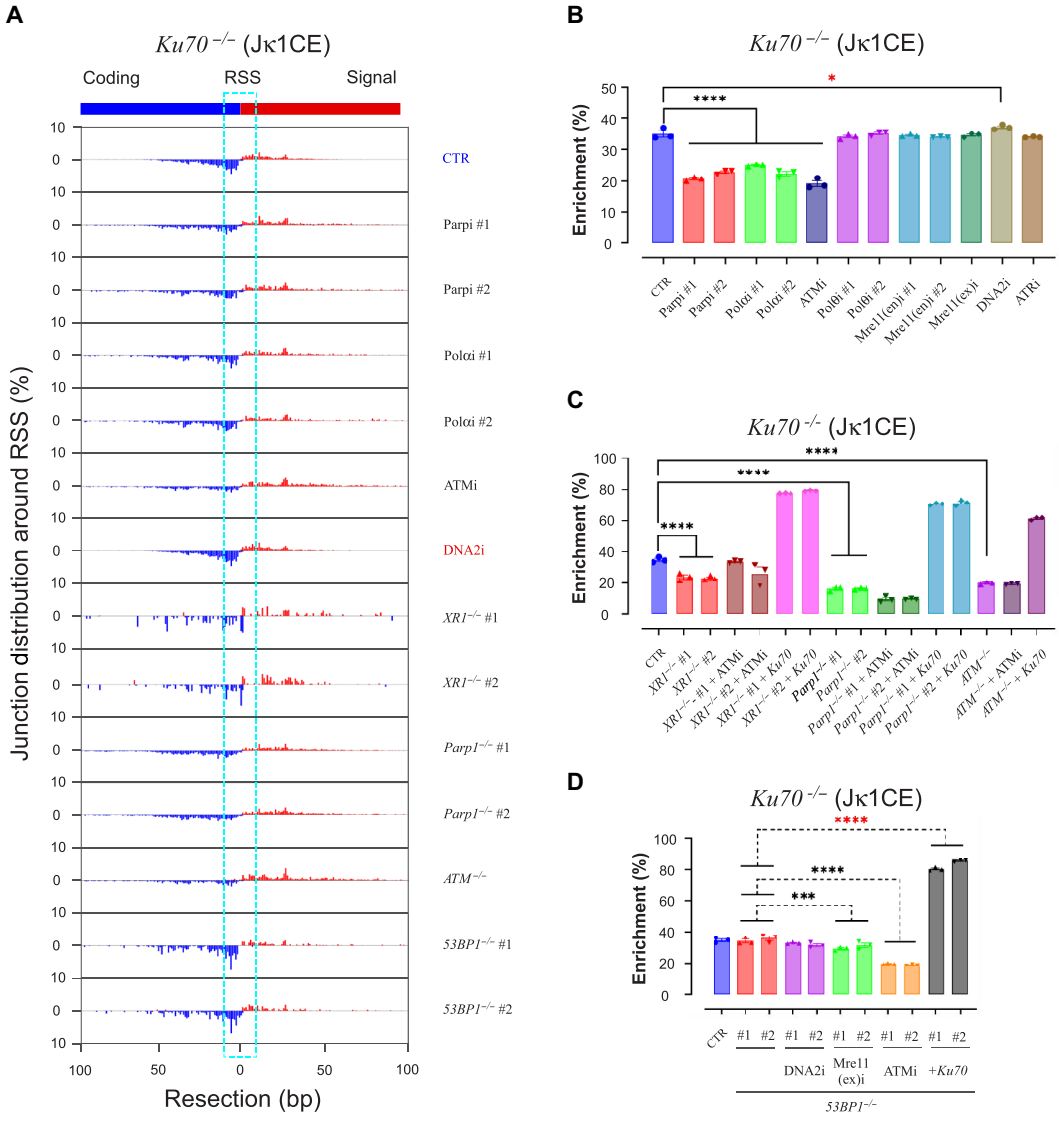

Fig. 3. A-EJ regulators and drivers, but not 53BP1, suppress hyper-resected joints. (**A**) Coding and signal prey junctions of Vκ region DSBs from the Jκ1CE bait are aggregated in a resection window of ±100 bp around the RAG1/2 DSB (RSS). Representative plots showing restricted (DNA2i treatment), extended (Polα inhibition; XR1 deletion; Parp1 and ATM inhibition or deletion), or no significant change (53BP1 deletion) are indicated. (**B** to **D**) The percentage of junctions that enriched in the window of ±10 bp around the RSS site was used as an indicator for resection, as cyan dashed rectangle in (A). The significance of enrichment changes when combined with indicated inhibitors or gene modification or both was evaluated by one-way ANOVA (B and C) and two-way ANOVA (D) plus posttest comparison; $N = 3$.

(Fig. 3, A and B, and fig. S10, A and B), which correlates with its impacts on V-J recombination efficiency. As predicted, restoration of NHEJ through Ku70 expression dropped the resected joint fraction by ~2-fold in relevant cell lines except those with additional LigIV deficiency (Fig. 3, C and D; figs. S10, C and D, and S11, A to F; and tables S3 and S4), which are subject to DNA-PK–mediated resection mechanisms (*49*). Collectively, we conclude that DNA2 promotes resected end joining while Parp1, XRCC1, Polα, and ATM signaling limit resected end joining in the absence of Ku70. We also conclude, counterintuitively, that 53BP1 does not influence resected joint distributions despite crucially supporting A-EJ recombination efficiency.

MMEJ increases with greater declines in A-EJ activity

As resection enhances the likelihood of relying on junctional MHs to stabilize/align ends and complete ligation, we wanted to know whether increased resected joints correlated with changes in Vκ region junction structure patterns. For a baseline A-EJ measure, $Ku70^{-/-}$ joints from either CE or SE baits contain very few insertions and have a dominant peak of direct joints (~50 to 60%), along with an exponential decay of increasing MH lengths (1 to 4 bp) (Fig. 4A). In contrast, NHEJ restoration via Ku70 complementation reduced MH use and increased direct repair and specifically increased palindromic insertions from CE baits, consistent with what is observed in WT *vAbl* cells (*4*, *49*, *50*) (Fig. 4, A to D, and figs. S12, A to F; S13, A and B; S14, A to D; and S15, A to D). For the A-EJ perturbations, both CE and SE bait junctions displayed similar pattern changes across comparisons with the 1-bp MH representing an inflection point from the $Ku70^{-/-}$ joint structure pattern. Of the 12 inhibitors, only ATM and Polα (#1/2) inhibitors increased total MMEJ (>1 bp) by ~100% while Parp (#1/2) inhibitors marginally increased MMEJ. $Ku70^{-/-}Atm^{-/-}$ cells also reproduced the phenotype of ATMi-mediated MMEJ increase. Although $Ku70^{-/-}Parp1^{-/-}$ (#1/2) structures were not altered, inclusion of ATMi promoted MMEJ synergy with a 30 to 40% transition of direct to MH joint utilization (Fig. 4, A and B, and fig. S12, A to D). However, when integrated with an unchanged resected joint pattern with combined Parp1 and ATM perturbation (Fig. 3C and fig. S10C), the data suggest that resection alone is not causal for the MMEJ synergy. Furthering this notion, $Ku70^{-/-}53bp1^{-/-}$ (#1/2) lines, which did not increase the range of resected joints, increased total MMEJ to a similar level as ATMi alone. Added Mre11, DNA2, or ATM inhibitors did not affect the increased MMEJ pattern (Fig. 4C and fig. S12E). A similar result for these inhibitors was observed in other 53BP1-deficient backgrounds, and Exo1 deficiency in the various backgrounds did not enhance MMEJ (figs. S13, A and B, and S15, A to D). A robust transition to MMEJ that was similar in phenotype to $Ku70^{-/-}Parp1^{-/-}$ + ATMi was revealed in $Ku70^{-/-}Xrcc1^{-/-}$ cells (#1/2) that used ~18% direct joints. In this regard, direct joint utilization was further reduced to ~8% with ATMi and is reminiscent of the G_0-G_1 phase $Lig4^{-/-}$ *vAbl* MMEJ pattern for both bait ends (*49*). Collectively, these observations imply that increased MMEJ does not necessarily rely on altered resected joint patterns, but rather, the altered patterns may be a consequence of increased MMEJ utilization. The data also support the concept that near-exclusive MMEJ utilization is suppressed by both the ATM-recruited 53BP1 chromatin domain and the bona fide A-EJ pathway.

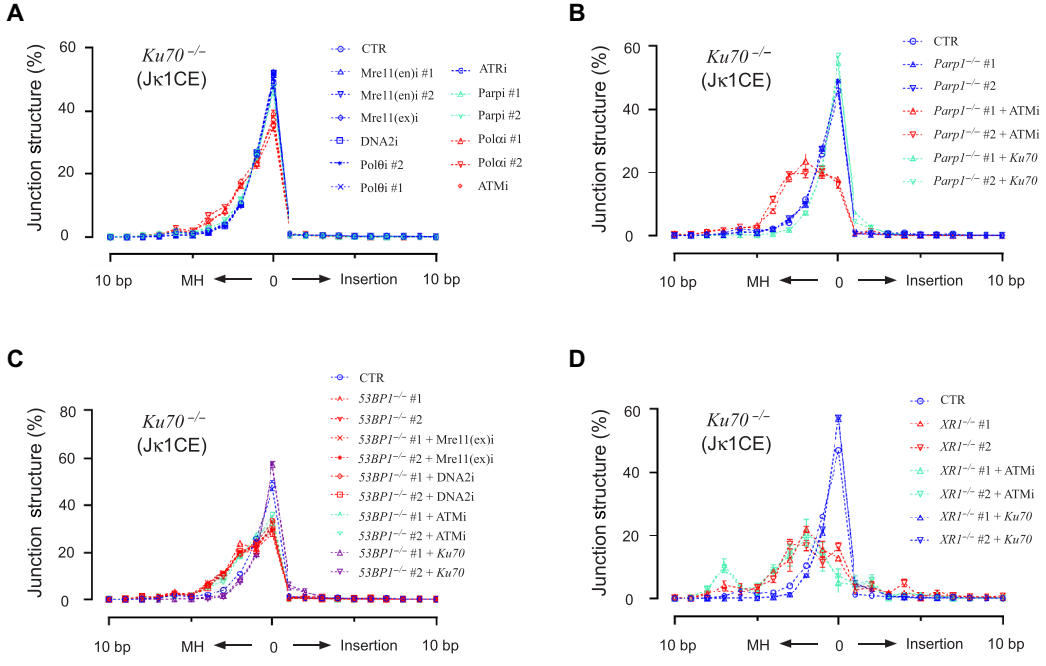

Fig. 4. MMEJ increases with greater declines in A-EJ function. (**A**) Jκ1CE bait and Vκ region prey junction structure distributions for the various inhibitors are split into three groups: no detectable pattern change (blue), marginal change (Parpi #1/2, green), and substantial change (Polαi #1/2 and ATMi). The repair profile was shown in the ±10-bp window, the left part indicates overlapping bait/prey microhomology (MH) length, 0 indicates direct (blunt) repair, and the right part indicates the insertion size. (**B** to **D**) Same as (A) but for Parp1, 53BP1, and XRCC1 deletion with or without the indicated inhibitors or Ku70 expression, respectively. All experiments were biologically repeated three times.

ATM and Parp1 maintain recombination fidelity

Given that the DDR supports A-EJ functions, we evaluated whether perturbing pathway components altered Vκ region CE and SE pairing to the Jκ1 bait DSB to further promote CE-SE hybrid joining. To do this, we quantified the number of junctions based on the joining types and derived the CE/SE ratio (Fig. 5A and tables S3 and S4). From the CE bait in WT *vAbl* cells, CE-CE recombination fidelity averaged ~850:1, and ATMi decreased bias ~18-fold, down to ~45:1 (fig. S16A and table S3) but remained dependent on NHEJ (*51*). Among the other inhibitors, only Parpi (#1/2) displayed an increase in these hybrid CE-SE joints, but this effect was only ~2-fold. Although the absence of Ku70 significantly drops CE recombination fidelity down to ~2:1 (*4*, *49*), we discovered that inhibited ATM and Parp had similar effects in further decreasing recombination fidelity toward a true translocation-defined 1:1 CE/SE ratio with no additional inhibitors affecting recombination fidelity (Fig. 5B). Similar to the trend of increased resected joints (Fig. 3, A to D), $Parp1^{-/-}$ (#1/2) and $Xrcc1^{-/-}$ (#1/2), but not $53bp1^{-/-}$ (#1/2) or $Exo1^{-/-}$ (#1/2/3), also decreased the residual end bias (Fig. 5, B and C, and fig. S16, B and C). However, while $Ku70^{-/-}Atm^{-/-}$ or $Ku70^{-/-}$ + ATMi dropped CE bias down to ~1:1, SE bias from the Jκ1SE bait increased ~3-fold to ~3:1 (Fig. 5, B and C, and tables S3 and S4); this ATMi effect to recover SE fidelity was also found across all combinations, including 53BP1 deficiency (table S4). This is notable because only ATM perturbation displayed both a CE bias drop and an SE bias rise in A-EJ backgrounds (tables S3 and S4), supporting prior work that ATM regulates RAG1/2 postcleavage activity in DNA-PK–deficient cells (*52*).

A-EJ and ATM increase distal Vκ recombination

The Igκ topologically associating domain (TAD) can be divided into Vκ region sub-TADs—*sTAD1-2*, *sTAD3*, *sTAD4*, and *sTAD5* (*53*), each with varying numbers of actively extruding CTCF/cohesion anchored chromatin loops that form an interaction zone for V-J pairing and cleavage by RAG1/2 (*54*). In *WT vAbl* cells, Jκ1CE bait recombination was the greatest in the Jκ proximal sTAD (*sTAD5*; ~45%) and declined as a function of linear distance with the distal sTAD (*sTAD1-2*) contributing ~11% of total recombination (fig. S17, A and B, and table S3). In contrast, $Ku70^{-/-}$ *vAbl* cells displayed a similar overall trend but with a ~7% decrease in *sTAD5* and ~7% increase in *sTAD1-2* (Fig. 6, A to C, and table S3). From the panel of inhibitors tested, none displayed a discernible shift in the landscape of utilization from WT cells (fig. S17B and tables S3 and S4). However, only ATMi or $Atm^{-/-}$ further increased sTAD1-2 recombination in $Ku70^{-/-}$ by ~5 to 6% (Fig. 6, B and C; fig. S18, A to C; and table S3) and was consistently found across other $Ku70^{-/-}$ combinations except for $Ku70^{-/-}Xrcc1^{-/-}$ (Fig. 6C and tables S3 and S4). We conclude that A-EJ and inhibited ATM have additive effects on promoting distal V-J recombination.

Compromised DDR affects A-EJ translocations

Despite the normally well-orchestrated process of V(D)J recombination, chromosome translocations between RAG1/2-mediated and spontaneous DSBs can also occur. Thus, we sought to determine whether genome-wide junctions are repaired similarly to recombined junctions in the Igκ locus in the context of A-EJ and DDR gene perturbation. In this regard, translocations represented a mix of spontaneous prey DSBs and RAG1/2 prey DSBs from other antigen receptor loci (e.g., Igλ, IgH, etc.). Therefore, we analyzed both the relative and absolute translocation pools (see Materials and Methods), which were highly correlated (tables S3 and S4), to describe notable changes. In general, WT translocations were low in frequency and composed mostly of spontaneous DSB end partners. Whereas $Ku70^{-/-}$ translocations were three- to sixfold higher in frequency with a greater proportion coming from other antigen receptor locus RAG1/2 DSB end partners (Fig. 7A, figs. S19A and S20A,

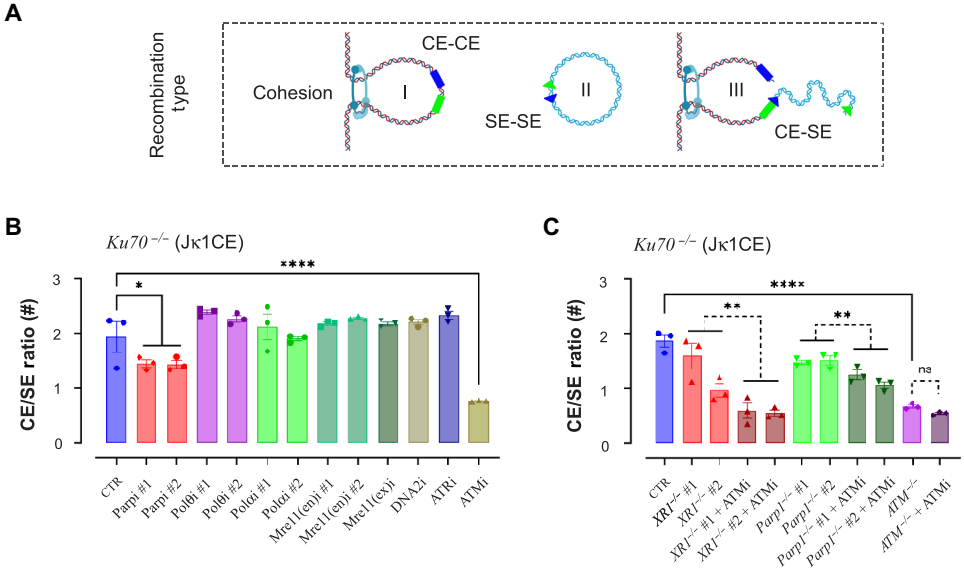

Fig. 5. ATM and Parp1 maintain recombination fidelity. (**A**) An illustration of possible recombination outcomes of post-RAG1/2 cleavage, including coding to coding (CE-CE) (I), signal to signal (SE-SE) (II), and hybrid joins (CE-SE) (III). (**B**) The $Ku70^{-/-}$ cell CE/SE ratio from Jκ1CE bait is indicated with or without the indicated inhibitors. (**C**) Same as (B) but with additional XRCC1 (XR1), Parp1, or ATM deletion with or without ATM inhibitor. One-way ANOVA with posttest significance for each comparison is indicated; $N = 3$. (A) was created with BioRender.com.

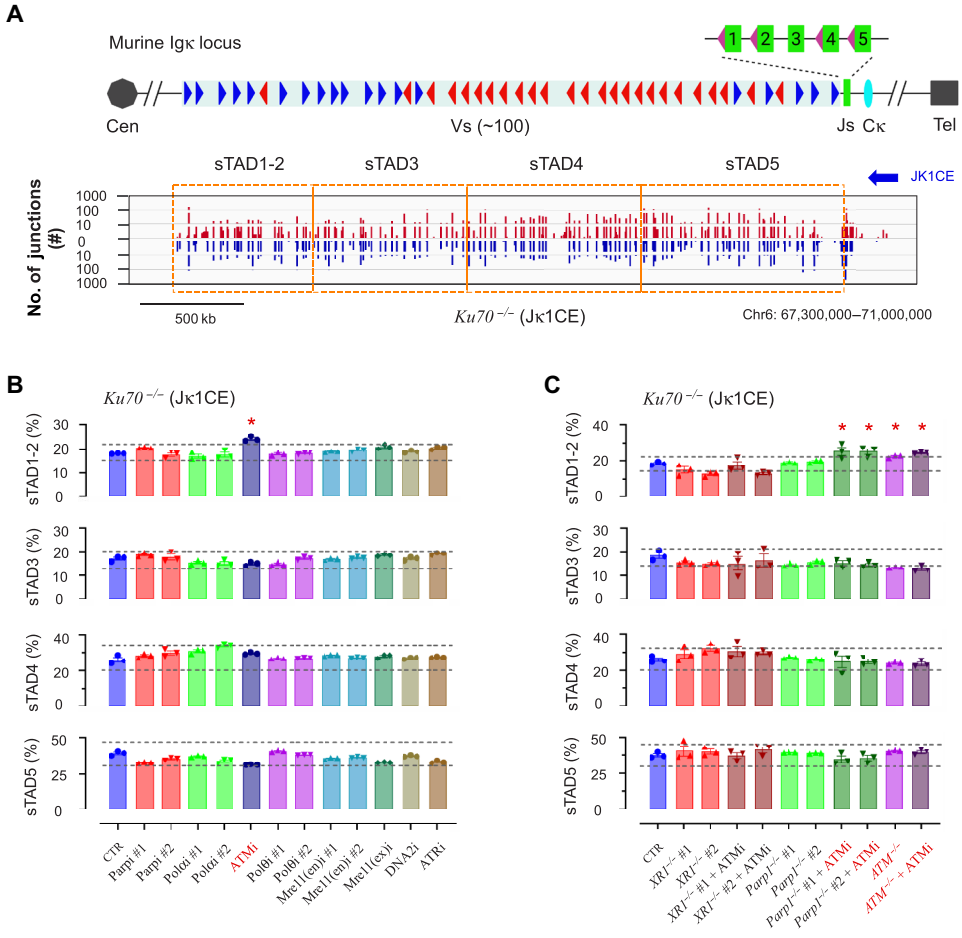

Fig. 6. A-EJ and ATM increase distal Vκ recombination. (**A**) The Igκ locus is a topologically associated domain (TAD) that can be divided into four subTADs: *sTAD1-2*, *sTAD3*, *sTAD4*, and *sTAD5* (*53*), as shown in the *Ku70*$^{-/-}$ Jκ1CE bait control. (**B**) The percentage of the four segments with or without indicated inhibitors as indicated. (**C**) Same as in (B) but for XRCC1 (XR1), Parp1, and ATM deletions with or without ATM inhibitor. Text highlighted in red and indicated in the graph by red asterisks denotes conditions that extend beyond the ±20% threshold change of the CTR (dashed lines). All experiments represent three biological replications. (A) generated from the Integrative Genomics Viewer (igv.org).

and tables S3 and S4). Consistent with the negative impact to V-J efficiency (fig. S4, B and C), WT *vAbl* cells treated with Parp, ATM, or ATR inhibitors increased translocations (fig. S19, A to H). Notably, *Ku70*$^{-/-}$ *vAbl* cells treated with Parpi (#1/2) specifically increased spontaneous translocations, while ATMi preferentially increased RAG1/2 translocations (fig. S19, B and D, and tables S3 and S4). This difference emphasizes their respective roles in base excision repair and regulating RAG1/2 recombination center activity. Unlike WT CE bait V-J joints that were predominantly direct with some insertions (~20%), WT CE bait translocation joints were primarily insertions (~70%) with a cascading enrichment of direct (~20%) and MHs (~10%). This pattern is consistent with coding end preservation and committed repair by NHEJ. In this context, many of the inhibitors increased direct and MH utilization, where the compounds that decreased V-J efficiency and increased translocations, like ATMi, Parpi, ATRi, and Polαi, also displayed the greatest MMEJ transition (fig. S19, I and J).

The chemical inhibition and gene deletion effects on *Ku70*$^{-/-}$ translocation frequency revealed both gains and losses. ATM deletion or inhibition of ATR, Mre11(ex), or ATM (including with all gene deletion contexts) consistently increased translocations (Fig. 7, A to E, and fig. S20, A and B), which, for the exception of Mre11(ex)i, corresponded with decreased V-J efficiencies (Fig. 1, B and C, and fig. S4, C and D). In contrast, deficiency of XRCC1 or 53BP1 recovered very few translocations (Fig. 7, A to F; figs. S20, A and B, and S21; and tables S3 and S4) consistent with robust decreases in V-J efficiencies (Figs. 1C and 2B and figs. S4D and S6B). Unlike with WT *vAbl* cells, Parpi or Parp1 deficiency in *Ku70*$^{-/-}$ *vAbl* cells did not change the translocation level. This unexpected effect may be normalized due to a combined genome-wide DSB increase and a partially compromised A-EJ. Joint structures of *Ku70*$^{-/-}$ translocations resembled V-region joint structures, and similar patterns emerged for all other added DDR or A-EJ perturbations (fig. S22, A to D). Notably, ATMi treatment in all measurable *Ku70*$^{-/-}$ double-knockout combinations generally doubled MMEJ utilization from the 20% baseline (fig. S22, C and D). However, the low translocation frequencies in the severely compromised backgrounds (i.e., *Ku70*$^{-/-}$*Xrcc1*$^{-/-}$ and *Ku70*$^{-/-}$*53bp1*$^{-/-}$) precluded further comparison. In summary, the data reveal two distinct groups of genes that

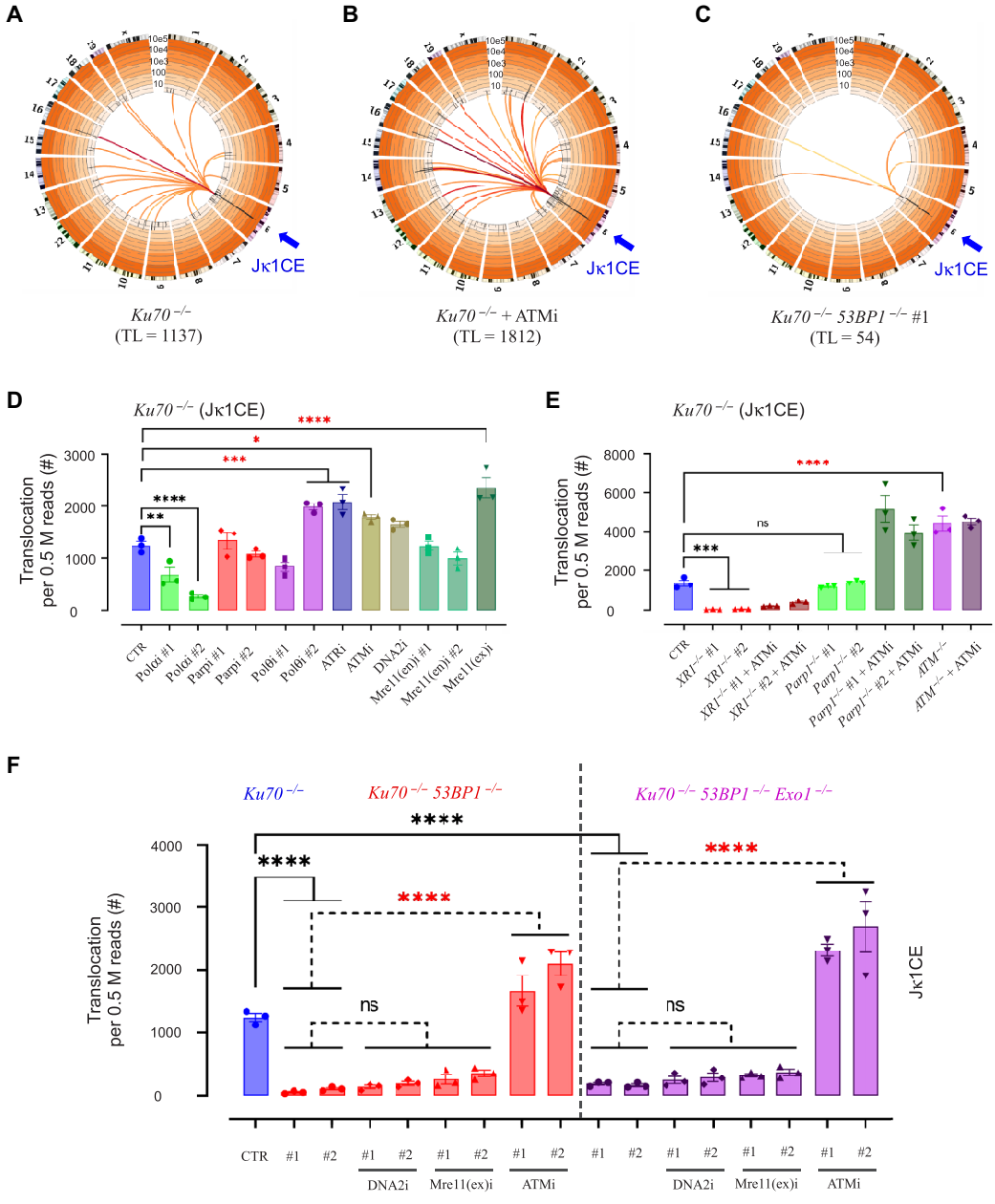

Fig. 7. Compromised DDR affects A-EJ translocations. (**A** to **C**) Representative genome-wide plots of junctions joined with Jκ1CE in *Ku70*$^{-/-}$ (A), *Ku70*$^{-/-}$ + ATMi (B), and *Ku70*$^{-/-}$ *53BP1*$^{-/-}$ #1 (C). (**D** to **F**) Relative translocation frequencies in *Ku70*$^{-/-}$ with or without the indicated inhibitors, deletions, or both per 0.5 M (million) sequence read pairs. The significance between *Ku70*$^{-/-}$ (CTR) and the indicated inhibitors, gene modification, or both was evaluated by one-way ANOVA plus posttest comparison: **P* < 0.05, ***P* < 0.01, ****P* < 0.001, *****P* < 0.0001; *N* = 3.

influence translocation generation: (i) upstream DDR genes that influence A-EJ synapsis partners, and (ii) end-joining capacity genes essential for the bona fide A-EJ pathway.

DISCUSSION

This study revealed Parp1 and XRCC1 as crucial A-EJ factors that drive Igκ V-J recombination and DSB repair in the absence of the Ku-initiated NHEJ. This mechanism is aided by the ATM-initiated DDR that stabilizes end joining via 53BP1. On the one hand, disrupting the core A-EJ factor XRCC1 decreases both V-J recombination and translocations, with residual joints consisting mostly of MHs to stabilize their end ligation. On the other hand, disrupting the DDR at different stages is varied, where key factor perturbations highlight defective end-joining fidelity, efficiency, and/or synapsis functions, most of which are also either evident with or functionally compensated by NHEJ (*41*, *55*). Thus, the short-range resection and repair that is associated with this A-EJ mechanism is an excellent model to understand the plasticity of the DDR, particularly from 53BP1-regulated and ATM-independent contexts,

to elucidate additional end-joining mechanisms (Fig. 8). Our data provide further insight into the regulation of this heir-apparent end-joining pathway.

Although its role(s) in A-EJ will need more clarity, poly(ADP) ribosylation contributed by Parp1 and Parp2 labels DNA end termini, histones, and DNA repair proteins (*56*, *57*) and, therefore, could facilitate end access, tethering at the nucleosome level or even end bridging (*58*, *59*). The likelihood of both genes operating in A-EJ is consistent with the partial loss in repair with Parp1 deficiency and a greater A-EJ defect with Parp inhibitors that preferentially trap Parp2 (*60*); however, functions in addition to A-EJ are likely the reason why dual deficiency of these genes is cell lethal in NHEJ-proficient *vAbl* cells (*61*). In this regard, Parp1/Parp2 functions in chromatin remodeling due to overlapping linker histone regulation with the DDR kinases (*62*, *63*) may explain its role in supporting both DNA end-joining mechanisms. Inhibiting ATM in *Ku70*$^{-/-}$ *Parp1*$^{-/-}$ cells had distinguishing phenotypes that were either synergistic (e.g., junction structures, translocations) or antagonistic (e.g., CE/SE ratio), with the latter involving an unscheduled release of SEs from the RAG1/2 postcleavage complex. Thus, the Parp1/ATM redundancy to remove linker histones by a combination of phosphorylation, ubiquitination, and parylation could be central to effectively joining DNA ends by the bona fide A-EJ mechanism.

Our data also imply that LigIII drives G_0-G_1 phase A-EJ. Loss of its chromatin loader, XRCC1, substantially reduces its protein expression, whereas LigI protein expression is heavily down-regulated at the onset of V(D)J recombination (*41*). The notable transition to more resected joints and increased MMEJ as a function of A-EJ loss implicates XRCC1 as the central scaffolding factor necessary to form direct or limited MH joints. This model is consistent with prior studies demonstrating that XRCC1 more rapidly accumulates at DNA strand breaks than the polymerase loader, PCNA (*64*, *65*), and the DDR (*66*). In the context of base excision repair (BER), XRCC1 recruitment to damaged sites is enhanced by Parp1 or Parp2 ADP ribosylation (*67*) and is a requisite component for polymerase beta (Polβ) recruitment (*68*) to enable limited fill-in activity. Curiously, Polλ acts to "back up" Polβ excision repair functions (*69*). Both polymerases display some level of MMEJ activity for short 3′ overhangs (*70*), which, for Polλ, could generate short and long MHs that are characteristic of NHEJ and Polθ-mediated end joining, respectively (*22*). Therefore, we speculate that A-EJ may use a similar BER polymerase preference, which may change with an increasing end destabilization burden.

With respect to how the DDR supports A-EJ, inactivation via ATM deletion or inhibition in *Ku70*$^{-/-}$ cells impaired A-EJ synapsis and enhanced MMEJ in all conditions, indicating a primary role to stabilize ends for ligation and preventing translocation (Fig. 8). The high functional overlap between the ATM perturbations for A-EJ is consistent with kinase-dead ATM versus deficiency having no overt difference in NHEJ-mediated V(D)J recombination despite kinase dead dominant effects to block topoisomerase I lesion resolution during replication as a putative causal mechanism for viability and cancer predisposition differences (*71*, *72*). Therefore, the difference in V-J efficiency between inhibited (decreased) and deficient (no change) ATM could be due to the ability of ATR to compensate for ATM absence, given that inhibited ATR also negatively affected V(D)J recombination while increasing translocations; further studies will be necessary to reveal unique and overlapping DDR kinase functions for A-EJ. However, the DDR's most notable impact on A-EJ was 53BP1 deficiency, which robustly suppressed V-J efficiency and translocations while increasing MMEJ yet not altering resected joint distributions. These observations suggest that the 53BP1 chromatin domain provides end stability and alignment to facilitate blunt (direct) end joining, as evidenced by the numerous

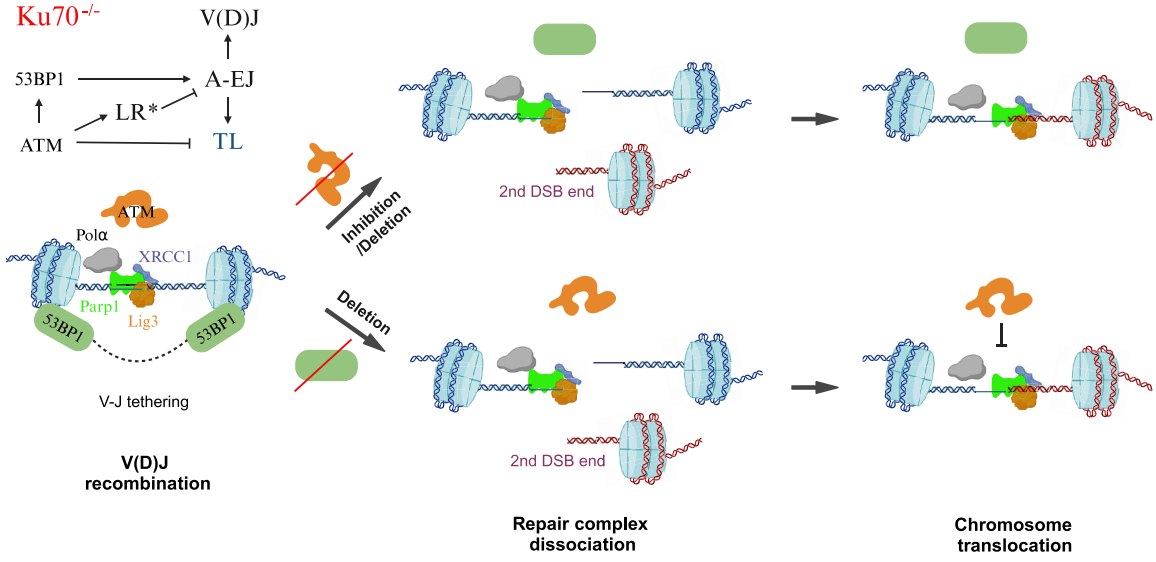

Fig. 8. ATM and 53BP1 regulate A-EJ–mediated V(D)J recombination and chromosome translocation. Ku70 deficiency eliminates NHEJ and enables a bona fide A-EJ mechanism involving Parp1, XRCC1, and LigIII to complete V(D)J recombination, initiated by the RAG1/2 endonuclease. A-EJ is supported by the ATM-mediated DDR which recruits 53BP1 to facilitate end salvage mechanisms (e.g., distal end tethering) and suppress the formation of translocations (TL). ATM also activates nucleases to promote long-range resection (LR*) and suppress A-EJ when 53BP1 is absent or excluded from DDR recruitment. Thus, inhibiting or deleting ATM (top) increases translocations due to diminished end tethering support and nuclease activation, while deleting 53BP1 (bottom) decreases overall A-EJ capacity by dissociating the V-J tethered repair complex and enabling ATM-activated nucleases to suppress translocations. Created with BioRender.com.

53BP1-associated complexes to regulate end processing (*31*,*35*–*37*, *39*), and presents a limited temporal window even for NHEJ to complete V(D)J recombination in its absence (*73*–*75*). Therefore, the residual A-EJ in the absence of 53BP1 likely reflects a kinetic component to DSB repair (i.e., fast ligation fraction). A corollary to the end stability provided by 53BP1 is that translocations are likely formed and perhaps synergized when persisting DSBs are fused into the same 53BP1 chromatin domain (*76*) as a necessary step to ensure that stable DNA ends are repaired even at the cost of rearrangement.

Our study complements recent work described by the Ceccaldi and Sfeir groups (*77*, *78*), which revealed a mitosis-specific DSB repair mechanism directed by the CDK1-activated polo-like kinase 1 (PLK1) to promote an ATM-dependent, but ATR-independent, MMEJ mechanism involving Polθ, TOPBP1, MDC1, the RAD9-RAD1-HUS1 DNA clamp complex, and its interacting partner, RHINO (Rad9, Rad1, Hus1 Interacting Nuclear Orphan). This mitotic DSB repair mechanism does not involve NHEJ or homologous recombination due to the negative regulation of 53BP1 and BRCA2 by the CDK1-PLK1 axis (*77*, *79*–*81*). As cells enter the G_1 phase, NHEJ proficiency returns, enabling 53BP1 nuclear bodies to form due to unresolved mitotic DNA damage. Polθ nuclear bodies also form, but both are nearly mutually excluded from each other (*77*), suggesting that Polθ largely operates external to the 53BP1 domain in early G_1 and is consistent with 53BP1 acting as a Polθ synthetic lethal partner (*12*, *82*). Although further investigation will determine the repair and end processing hierarchy, we propose that the bona fide A-EJ mechanism is functionally distinct from the Polθ-mediated A-EJ mechanism and speculate that most of the MMEJ outcomes described here for A-EJ, elsewhere for *Lig4*$^{-/-}$ (*4*, *49*), and in cycling cell contexts represent repair events beyond the regulation of 53BP1.

An added complication to this study is the regulation of the RAG1/2 postcleavage synaptic complex by ATM and how these ends are handed off to repair pathways. Coding ends are first released from the RAG1/2 complex to complete repair by NHEJ, while the release of signal ends for repair occurs afterward. For the latter part, RAG2 phosphorylation by ATM suppresses the release of signal ends (*52*) to minimize bi-allelic cleavage (*83*). Therefore, premature signal end release as coding ends are processed would disrupt DNA-PK synapsis and generate more re-synapsed and ligated hybrid joints (*41*). In support of this model, our WT + ATMi *vAbl* data indicate that signal ends are subjected to similar end processing as their fated coding-end partner, indicating that re-synapsis occurs before most hairpins are opened. Furthermore, while the increased level of rejoined Jκ1 DSB ends occur in the absence of Ku70, ATMi in WT cells does not substantially promote this type of activity; rather, we find ~10-fold increased inversional J-J coding joints to all Jκ DSBs in the Jκ recombination center, which, given this high frequency relative to translocations to other antigen receptor loci (table S3), suggests that ATM regulates postcleavage activity of multiply loaded RAG1/2 sites within a single Jκ recombination center. Therefore, with respect to A-EJ and the generation of substantially more hybrid joints, we propose that the kinetics of signal end acquisition by A-EJ are faster than ATM recruitment (*66*) for most postcleavage complexes, reflecting the modest increase in hybrid joints with additional ATM inhibition.

MATERIALS AND METHODS

Cell lines

Mouse *vAbl* cells including WT (clone B), *L4*$^{-/-}$, *Ku70*$^{-/-}$, and *L4*$^{-/-}$ *Ku70*$^{-/-}$ (*K7L4*$^{-/-}$) cells were reported in our previous study (*4*). Putative A-EJ and DDR genes were deleted in the Ku70-deficient (clone B1) or the *Lig4*$^{-/-}$*Ku70*$^{-/-}$ (clone A1–1) *vAbl* lines to generate the following lines: *Ku70*$^{-/-}$*Atm*$^{-/-}$, *Ku70*$^{-/-}$*Xrcc1*$^{-/-}$, *Ku70*$^{-/-}$*53bp1*$^{-/-}$, *Ku70*$^{-/-}$*Parp1*$^{-/-}$, *Ku70*$^{-/-}$*Exo1*$^{-/-}$, *Ku70*$^{-/-}$*53bp1*$^{-/-}$*Exo1*$^{-/-}$, and *Lig4*$^{-/-}$*Ku70*$^{-/-}$*53bp1*$^{-/-}$. Ku70 was ectopically expressed in *Ku70*$^{-/-}$-related cell lines using lenti-iKu70-GFP. Confirmation of these cell lines was performed by genotyping using the primers listed in table S5 and Western blotting using the antibody indicated. All *vAbl* cells were cultured at 37°C and 5% CO_2 in RPMI 1640 medium supplemented with 10% (v/v) fetal bovine serum, penicillin/streptomycin (50 U/ml), 2 mM L-glutamine, 1× MEM nonessential amino acids (NEAA), 1 mM sodium pyruvate, 50 μM 2-mercaptoethanol, and 20 mM Hepes (pH 7.4). To induce V(D)J recombination, *vAbl* cells were seeded at a concentration of 1 million cells/ml and supplemented with 3 μM STI-571 for 4 days. Cells treated with STI-571 were not used for cell line preservation.

Compounds

The following compounds and their intended effects are indicated: G_1-G_0 arrest—STI-571 (3 μM, TCI Chemicals, catalog no. TCI0936-100MG); Cell cycle analysis—EdU (50 μM, Cayman, catalog no. 20518); Inducible gene expression—Doxycycline (2 μM, Sigma-Aldrich, catalog no. D9891-10G); Parp inhibition—Olaparib [Parpi #1, 10 μM (*84*, *85*), AdooQ BioScience, catalog no. A10111] and Talazoparib [Parpi #2, 1 μM (*86*, *87*), ApexBio, catalog no. A4153]; Polθ inhibition—Novobiocin [Polθi #1, 100 μM (*88*), BioVision, catalog no. B1526-1G] and ART558 [Polθi #2, 10 μM (*89*), MedChem Express, catalog no. HY-141520]; Polα inhibition—Adarotene [Polαi #1, 1 μM (*39*, *90*), MedChem Express, catalog no. HY-14808] and CD437 [Polαi #2, 5 μM (*91*), Sigma-Aldrich, catalog no. 178496-5MG]; ATR inhibition—AZD6738 [ATRi, 0.5 μM (*92*), MedChem Express, catalog no. HY-19323]; ATM inhibition—Ku60019 [ATMi, 2 μM (*93*), Sigma-Aldrich, catalog no. SML1416-5MG]; DNA2 inhibition—C5 [DNA2i, 20 μM (*94*), MedChem Express, catalog no. HY-128729]; Mre11 inhibition—PFM01 (Mre11eni #1, 10 μM), PFM03 (Mre11eni #2, 10 μM), and PFM39 (Mre11exi, 100 μM) were from the Tainer laboratory (*95*).

Gene knockout using CRISPR-Cas9

The genes indicated in this study were knockout using paired guide RNAs. In brief, 5 μl of 20 μM crRNA was mixed with 5 μl of 20 μM tracrRNA, denatured at 90°C for 2 min, and annealed at room temperature for 30 min to form guide RNA. Five microliters of 10 μM guide RNA was mixed with 0.5 μl of 5× PBS buffer (RNase-free) and 0.5 μl of 60 μM SpCas9 protein and incubated at room temperature for 10 min. Paired guide RNPs were mixed with nucleofection buffer (SF Cell Line 4D X Kit, Lonza, #V4XC-2024) and delivered into 10 million vAbl cells using 4D-nucleofector system (Lonza, Core plus X unit).

Lentivirus production

Lentivirus containing ihKu70-GFP-Blast cassette was generated using the second generation lentivirus packaging system as described previously (*49*). The lentivirus titration was recommended to be performed in the targeting cell lines rather than in HEK293T cells alone. Lentivirus was added into *vAbl* cells and maintained in R10 media with polybrene (5 μg/ml) for 2 days and changing media and continually cultured in R10 media with blasticidin (5 μg/ml) for 1 to 2 weeks (media were changed every 2 to 3 days to maintain the cell density between 0.1 and 2 million/ml).

Plenti-ihKu70-GFP-blast generation

The Human Ku70 gene was incorporated into the Lenti-iCas9-neo plasmid (Addgene #85400) through a two-step cloning process. Initially, the neomycin-resistant gene was substituted with a blasticidin-resistant gene. Subsequently, the Cas9 gene was replaced with the Ku70 gene.

Immunoblotting

The samples, including *vAbl Ku70*$^{-/-}$, *Ku70*$^{-/-}$*Xrcc1*$^{-/-}$ (#1/2), *Ku70*$^{-/-}$*Atm*$^{-/-}$ (#1/2), *Lig4*$^{-/-}$*Ku70*$^{-/-}$, and *Lig4*$^{-/-}$*Ku70*$^{-/-}$*53bp1*$^{-/-}$ (#1/2), were collected at a concentration of 5 million cells, spun down, and washed by 1 ml of RS buffer (150 mM NaCl and 10 mM tris, pH 7.5), spun down, resuspended using 100 μl of standard radioimmunoprecipitation assay lysis buffer (150 mM NaCl, 1% NP-40, 0.5% sodium deoxycholate, 0.1% SDS, and 50 mM tris, pH 8.0), and left on ice for 15 min; then, 100 μl of 2× Laemmli buffer (4% SDS, 5% 2-mercaptoethanol, 20% glycerol, 0.004% bromophenol blue, and 125 mM tris, pH 6.8) was added and incubated at 95°C for 10 min. Protein electrophoresis, membrane transfer, and immunoblotting were performed as previously described (*49*) using the following antibodies: anti-53BP1 (1:2000, Novus Biologicals #NBP2-54753SS), anti-ATM (1:1000, Proteintech #27156-1-AP), anti-LigI (1:1000, Proteintech #18051–1-AP), anti-LigIII (1:5000, BD Biosciences #BD611876), anti–Rabbit-immunoglobulin G (IgG) (1:2000, Thermo Fisher Scientific #G-21234), and anti-β-actin (1:4000, Santa Cruz Biotechnology #SC-47778).

Flow cytometry sorting

The *vAbl* cells that transfected with iKu70-GFP were induced by 3 μM Doxycycline at least 2 days before flow cytometry. The population expressed with iKu70-GFP was detected in fluorescein isothiocyanate channel and collected in a tube with R10 media. The selected cells were cultured for the experiments in this study.

HTGTS library preparation

HTGTS library preparation was performed as previously described (*43*, *49*) with some modifications. In brief, 5.5 μg of genomic DNA from each treatment condition was adjusted to 110 μl (50 ng/μl) and sheared using a bioruptor sonication device (Diagenode) in low mode for two cycles (30 s on + 60 s off) at 4°C, resulting in fragments ranging from 200 bp to 2 kb. The sheared fragments were transferred into a 96-well microplate and subjected to linear amplification (LAM)–PCR using biotin-labeled primers, including Bio-IgkJ1CE and Bio-IgkJ1SE proximal to the IgkJ1 RAG1/2 incision site, respectively. The LAM-PCR products were enriched using a streptavidin-coated 96-well microplate, followed by in situ adapter ligation. Unligated adapters were removed, and the ligated products were subjected to nested PCR using a common primer (AP2I7-novo) matching the adapter sequence and another barcoded I5 primer that matches the region between the bait site and the biotin-labeled primer. The DNA from the nested PCR was purified using SPRIselect beads (Beckman #B23318). Subsequently, tagged PCR was performed using primers P7I7 and P5I5, which match the primers used in the nested PCR. The PCR products were purified by 1% agarose gel electrophoresis, and DNA products with a length of 500 bp to 1 kb were excised and extracted using a gel extraction kit. The tagged DNA libraries were subjected to bioanalyzer analysis for quality control and sequencing using the Illumina NovaSeq-PE150. Please refer to table S6 for the oligos used.

Data analyses

LAM-HTGTS data analysis was performed following previously reported methods (*4*, *43*, *49*). Briefly, sequencing reads from Illumina NovaSeq PE150 were demultiplexed based on the inner barcodes and the sequence between the bait site and the nested PCR I5 primers using the fastq-multx tool from ea-utils. The adapter sequences were trimmed using the SeqPrep utility. The demultiplexing and trimming functions were integrated into a script called TranslocPreprocess.pl. Subsequently, the read pairs were normalized down to 500,000 using Seqtk and mapped to the mm9 reference genome using TranslocWrapper.pl to identify chromosome translocations or V-J recombination events, generating result tlx files. Relative translocation measurements were generated like V-J recombination joints by using the no-dedup option from TranslocWrapper.pl (*43*, *96*), whereas absolute translocation measures for junction structures were derived using default settings (*4*, *43*). Junctions that aligned to the bait region were not shown in the result tlx files and were extracted separately using a script called JoinT.R, resulting in JoinT tlx files containing translocations, V(D)J recombination, and rejoin events of the IgkJ1 region.

JoinT tlx files were converted into bedgraph files using tlx2bed.py, which were then visualized and plotted using IGV (integrative genomics viewer). Junctions in regions of interest from the JoinT tlx files were extracted using tlxbedintersect.py, which relied on two other scripts, tlx2BED.pl and pullTLXFromBED.pl. The regions of interest varied depending on the specific questions. For Vκ-Jκ recombination, the regions of interest were the RAG1/2 cleavage sites of Vκ genes, with a flanking 200-bp window (±200), which could be further divided into four to five TADs. In the case of translocation, the region of interest was the "prey" locus in all chromosomes except chr6. To visualize the relative translocation distributions, the representative JoinT tlx files were converted into circos plots.

The JoinT tlx files were also utilized for repair efficiency, pathway, and resection analyses. V-J efficiency (Vs% in tables S3 and S4) was calculated by dividing the junctions recovered from the Vκ region by the normalized total reads. JctStructure.R was used to determine the repair patterns, including MH, direct repair, and insertion over a range of 20 bp for each extreme. The degree of DSB end resection, indicated by the distribution of junctions near the DSB break site, was quantified using ResectionRSS.R.

Data obtained from Western blot and flow cytometry experiments were analyzed using ImageJ (NIH) and FlowJo (FlowJo LLC), respectively.

Software/code availability

All essential HTGTS-specific codes are described elsewhere (*4*, *43*, *49*) or are publicly available at https://zenodo.org/records/11099892 or https://github.com/JinglongSoM/LAM-HTGTS. The codes and software used in this study are indicated: Python (v3.8.5), R (v4.0.3), ImageJ, IGV (v2.8.2), and FlowJo (v10.8).

Statistical analysis

Data are reported as mean ± SEM unless specified otherwise. Differences were analyzed using one-way and two-way analysis of variance (ANOVA), followed by Dunnett's multiple comparisons test. Statistical calculations were carried out using GraphPad Prism 10 (GraphPad Software Inc.). A *P* value of less than 0.05 was deemed statistically significant.

Supplementary Materials

This PDF file includes:
Figs. S1 to S22
Legends for tables S1 to S6

Other Supplementary Material for this manuscript includes the following:
Tables S1 to S6

REFERENCES AND NOTES

1. Y. Zhang, X. Zhang, H.-Q. Dai, H. Hu, F. W. Alt, The role of chromatin loop extrusion in antibody diversification. *Nat. Rev. Immunol.* **22**, 550–566 (2022).
2. D. G. Schatz, Y. Ji, Recombination centres and the orchestration of V(D)J recombination. *Nat. Rev. Immunol.* **11**, 251–263 (2011).
3. W. Yu, C. Lescale, L. Babin, M. Bedora-Faure, H. Lenden-Hasse, L. Baron, C. Demangel, J. Yelamos, E. Brunet, L. Deriano, Repair of G1 induced DNA double-strand breaks in S-G2/M by alternative NHEJ. *Nat. Commun.* **11**, 5239 (2020).
4. Z. Liang, V. Kumar, M. Le Bouteiller, J. Zurita, J. Kenrick, S. G. Lin, J. Lou, J. Hu, A. Y. Ye, C. Boboila, F. W. Alt, R. L. Frock, Ku70 suppresses alternative end joining in G1-arrested progenitor B cells. *Proc. Natl. Acad. Sci. U.S.A.* **118**, e2103630118 (2021).
5. Q. Liu, L. Palomero, J. Moore, I. Guix, R. Espín, A. Aytés, J.-H. Mao, A. G. Paulovich, J. R. Whiteaker, R. G. Ivey, G. Iliakis, D. Luo, A. J. Chalmers, J. Murnane, M. A. Pujana, M. H. Barcellos-Hoff, Loss of TGFβ signaling increases alternative end-joining DNA repair that sensitizes to genotoxic therapies across cancer types. *Sci. Transl. Med.* **13**, eabc4465 (2021).
6. M. Audebert, B. Salles, P. Calsou, Involvement of poly(ADP-ribose) polymerase-1 and XRCC1/DNA ligase III in an alternative route for DNA double-strand breaks rejoining. *J. Biol. Chem.* **279**, 55117–55126 (2004).
7. M. Wang, W. Wu, W. Wu, B. Rosidi, L. Zhang, H. Wang, G. Iliakis, PARP-1 and Ku compete for repair of DNA double strand breaks by distinct NHEJ pathways. *Nucleic Acids Res.* **34**, 6170–6182 (2006).
8. D. Simsek, E. Brunet, S. Y.-W. Wong, S. Katyal, Y. Gao, P. J. McKinnon, J. Lou, L. Zhang, J. Li, E. J. Rebar, P. D. Gregory, M. C. Holmes, M. Jasin, DNA ligase III promotes alternative nonhomologous end-joining during chromosomal translocation formation. *PLOS Genet.* **7**, e1002080 (2011).
9. C. Boboila, V. Oksenych, M. Gostissa, J. H. Wang, S. Zha, Y. Zhang, H. Chai, C.-S. Lee, M. Jankovic, L.-M. A. Saez, M. C. Nussenzweig, P. J. McKinnon, F. W. Alt, B. Schwer, Robust chromosomal DNA repair via alternative end-joining in the absence of X-ray repair cross-complementing protein 1 (XRCC1). *Proc. Natl. Acad. Sci. U.S.A.* **109**, 2473–2478 (2012).
10. G. Lu, J. Duan, S. Shu, X. Wang, L. Gao, J. Guo, Y. Zhang, Ligase I and ligase III mediate the DNA double-strand break ligation in alternative end-joining. *Proc. Natl. Acad. Sci. U.S.A.* **113**, 1256–1260 (2016).
11. P. A. Mateos-Gomez, F. Gong, N. Nair, K. M. Miller, E. Lazzerini-Denchi, A. Sfeir, Mammalian polymerase θ promotes alternative NHEJ and suppresses recombination. *Nature* **518**, 254–257 (2015).
12. D. W. Wyatt, W. Feng, M. P. Conlin, M. J. Yousefzadeh, S. A. Roberts, P. Mieczkowski, R. D. Wood, G. P. Gupta, D. A. Ramsden, Essential roles for polymerase θ-mediated end joining in the repair of chromosome breaks. *Mol. Cell* **63**, 662–673 (2016).
13. Y. Zhang, M. Jasin, An essential role for CtIP in chromosomal translocation formation through an alternative end-joining pathway. *Nat. Struct. Mol. Biol.* **18**, 80–84 (2011).
14. M. Dinkelmann, E. Spehalski, T. Stoneham, J. Buis, Y. Wu, J. M. Sekiguchi, D. O. Ferguson, Multiple functions of MRN in end-joining pathways during isotype class switching. *Nat. Struct. Mol. Biol.* **16**, 808–813 (2009).
15. A. Xie, A. Kwok, R. Scully, Role of mammalian Mre11 in classical and alternative nonhomologous end joining. *Nat. Struct. Mol. Biol.* **16**, 814–818 (2009).
16. M. Lee-Theilen, A. J. Matthews, D. Kelly, S. Zheng, J. Chaudhuri, CtIP promotes microhomology-mediated alternative end joining during class-switch recombination. *Nat. Struct. Mol. Biol.* **18**, 75–79 (2011).
17. O. Barton, S. C. Naumann, R. Diemer-Biehs, J. Künzel, M. Steinlage, S. Conrad, N. Makharashvili, J. Wang, L. Feng, B. S. Lopez, T. T. Paull, J. Chen, P. A. Jeggo, M. Löbrich, Polo-like kinase 3 regulates CtIP during DNA double-strand break repair in G1. *J. Cell Biol.* **206**, 877–894 (2014).
18. F. Zheng, R. Georgescu, N. Y. Yao, H. Li, M. E. O'Donnell, Cryo-EM structures reveal that RFC recognizes both the 3′- and 5′-DNA ends to load PCNA onto gaps for DNA repair. *eLife* **11**, e77469 (2022).
19. F. Zheng, R. E. Georgescu, N. Y. Yao, M. E. O'Donnell, H. Li, Structures of 9-1-1 DNA checkpoint clamp loading at gaps from start to finish and ramification on biology. *Cell Rep.* **42**, 112694 (2023).
20. S. H. Chan, A. M. Yu, M. McVey, Dual roles for DNA polymerase theta in alternative end-joining repair of double-strand breaks in *Drosophila*. *PLOS Genet.* **6**, e1001005 (2010).
21. W. Koole, R. van Schendel, A. E. Karambelas, J. T. van Heteren, K. L. Okihara, M. Tijsterman, A polymerase theta-dependent repair pathway suppresses extensive genomic instability at endogenous G4 DNA sites. *Nat. Commun.* **5**, 3216 (2014).
22. G. Chandramouly, J. Jamsen, N. Borisonnik, M. Tyagi, M. L. Calbert, T. Tredinnick, A. Y. Ozdemir, T. Kent, E. V. Demidova, S. Arora, S. H. Wilson, R. T. Pomerantz, Polλ promotes microhomology-mediated end-joining. *Nat. Struct. Mol. Biol.* **30**, 107–114 (2023).
23. R. A. Deshpande, J.-H. Lee, S. Arora, T. T. Paull, Nbs1 converts the human Mre11/Rad50 nuclease complex into an endo/exonuclease machine specific for protein-DNA adducts. *Mol. Cell* **64**, 593–606 (2016).
24. P. Chanut, S. Britton, J. Coates, S. P. Jackson, P. Calsou, Coordinated nuclease activities counteract Ku at single-ended DNA double-strand breaks. *Nat. Commun.* **7**, 12889 (2016).
25. R. Anand, L. Ranjha, E. Cannavo, P. Cejka, Phosphorylated CtIP functions as a co-factor of the MRE11-RAD50-NBS1 endonuclease in DNA end resection. *Mol. Cell* **64**, 940–950 (2016).
26. R. Anand, A. Jasrotia, D. Bundschuh, S. M. Howard, L. Ranjha, M. Stucki, P. Cejka, NBS1 promotes the endonuclease activity of the MRE11-RAD50 complex by sensing CtIP phosphorylation. *EMBO J.* **38**, e101005 (2019).
27. S. C. Paudyal, S. Li, H. Yan, T. Hunter, Z. You, Dna2 initiates resection at clean DNA double-strand breaks. *Nucleic Acids Res.* **45**, 11766–11781 (2017).
28. W. D. Wright, S. S. Shah, W.-D. Heyer, Homologous recombination and the repair of DNA double-strand breaks. *J. Biol. Chem.* **293**, 10524–10535 (2018).
29. R. M. Densham, J. R. Morris, Moving mountains—The BRCA1 promotion of DNA resection. *Front. Mol. Biosci.* **6**, 79 (2019).
30. I. Ceppi, S. M. Howard, K. Kasaciunaite, C. Pinto, R. Anand, R. Seidel, P. Cejka, CtIP promotes the motor activity of DNA2 to accelerate long-range DNA end resection. *Proc. Natl. Acad. Sci. U.S.A.* **117**, 8859–8869 (2020).
31. S. M. Noordermeer, S. Adam, D. Setiaputra, M. Barazas, S. J. Pettitt, A. K. Ling, M. Olivieri, A. Álvarez-Quilón, N. Moatti, M. Zimmermann, S. Annunziato, D. B. Krastev, F. Song, I. Brandsma, J. Frankum, R. Brough, A. Sherker, S. Landry, R. K. Szilard, M. M. Munro, A. McEwan, T. Goullet de Rugy, Z.-Y. Lin, T. Hart, J. Moffat, A.-C. Gingras, A. Martin, H. van Attikum, J. Jonkers, C. J. Lord, S. Rottenberg, D. Durocher, The shieldin complex mediates 53BP1-dependent DNA repair. *Nature* **560**, 117–121 (2018).
32. H. Dev, T.-W. W. Chiang, C. Lescale, I. de Krijger, A. G. Martin, D. Pilger, J. Coates, M. Sczaniecka-Clift, W. Wei, M. Ostermaier, M. Herzog, J. Lam, A. Shea, M. Demir, Q. Wu, F. Yang, B. Fu, Z. Lai, G. Balmus, R. Belotserkovskaya, V. Serra, M. J. O'Connor, A. Bruna, P. Beli, L. Pellegrini, C. Caldas, L. Deriano, J. J. L. Jacobs, Y. Galanty, S. P. Jackson, Shieldin complex promotes DNA end-joining and counters homologous recombination in BRCA1-null cells. *Nat. Cell Biol.* **20**, 954–965 (2018).
33. S. Findlay, J. Heath, V. M. Luo, A. Malina, T. Morin, Y. Coulombe, B. Djerir, Z. Li, A. Samiei, E. Simo-Cheyou, M. Karam, H. Bagci, D. Rahat, D. Grapton, E. G. Lavoie, C. Dove, H. Khaled, H. Kuasne, K. K. Mann, K. O. Klein, C. M. Greenwood, Y. Tabach, M. Park, J.-F. Côté, J.-Y. Masson, A. Maréchal, A. Orthwein, SHLD2/FAM35A co-operates with REV7 to coordinate DNA double-strand break repair pathway choice. *EMBO J.* **37**, e100158 (2018).
34. M. Barazas, S. Annunziato, S. J. Pettitt, I. de Krijger, H. Ghezraoui, S. J. Roobol, C. Lutz, J. Frankum, F. F. Song, R. Brough, B. Evers, E. Gogola, J. Bhin, M. van de Ven, D. C. van Gent, J. J. L. Jacobs, R. Chapman, C. J. Lord, J. Jonkers, S. Rottenberg, The CST complex mediates end protection at double-strand breaks and promotes PARP inhibitor sensitivity in BRCA1-deficient cells. *Cell Rep.* **23**, 2107–2118 (2018).
35. Z. Mirman, F. Lottersberger, H. Takai, T. Kibe, Y. Gong, K. Takai, A. Bianchi, M. Zimmermann, D. Durocher, T. de Lange, 53BP1-RIF1-shieldin counteracts DSB resection through CST- and Polα-dependent fill-in. *Nature* **560**, 112–116 (2018).
36. N. Bigot, M. Day, R. A. Baldock, F. Z. Watts, A. W. Oliver, L. H. Pearl, Phosphorylation-mediated interactions with TOPBP1 couple 53BP1 and 9-1-1 to control the G1 DNA damage checkpoint. *eLife* **8**, e44353 (2019).
37. M. L. Swift, R. Zhou, A. Syed, L. A. Moreau, B. Tomasik, J. A. Tainer, P. A. Konstantinopoulos, A. D. D'Andrea, Y. J. He, D. Chowdhury, Dynamics of the DYNLL1-MRE11 complex regulate DNA end resection and recruitment of Shieldin to DSBs. *Nat. Struct. Mol. Biol.* **30**, 1456–1467 (2023).
38. J. Wang, A. Aroumougame, M. Lobrich, Y. Li, D. Chen, J. Chen, Z. Gong, PTIP associates with Artemis to dictate DNA repair pathway choice. *Genes Dev.* **28**, 2693–2698 (2014).
39. J. Paiano, N. Zolnerowich, W. Wu, R. Pavani, C. Wang, H. Li, L. Zheng, B. Shen, B. P. Sleckman, B.-R. Chen, A. Nussenzweig, Role of 53BP1 in end protection and DNA synthesis at DNA breaks. *Genes Dev.* **35**, 1356–1367 (2021).
40. A. T. Tubbs, Y. Dorsett, E. Chan, B. Helmink, B.-S. Lee, P. Hung, R. George, A. L. Bredemeyer, A. Mittal, R. V. Pappu, D. Chowdhury, N. Mosammaparast, M. S. Krangel, B. P. Sleckman, KAP-1 promotes resection of broken DNA ends not protected by γ-H2AX and 53BP1 in G_1-phase lymphocytes. *Mol. Cell. Biol.* **34**, 2811–2821 (2014).
41. A. L. Bredemeyer, G. G. Sharma, C.-Y. Huang, B. A. Helmink, L. M. Walker, K. C. Khor, B. Nuskey, K. E. Sullivan, T. K. Pandita, C. H. Bassing, B. P. Sleckman, ATM stabilizes DNA double-strand-break complexes during V(D)J recombination. *Nature* **442**, 466–470 (2006).
42. V. Kumar, F. W. Alt, R. L. Frock, PAXX and XLF DNA repair factors are functionally redundant in joining DNA breaks in a G1-arrested progenitor B-cell line. *Proc. Natl. Acad. Sci. U.S.A.* **113**, 10619–10624 (2016).

43. J. Hu, R. M. Meyers, J. Dong, R. A. Panchakshari, F. W. Alt, R. L. Frock, Detecting DNA double-stranded breaks in mammalian genomes by linear amplification-mediated high-throughput genome-wide translocation sequencing. *Nat. Protoc.* **11**, 853–871 (2016).
44. J. M. May, T. W. Owens, M. D. Mandler, B. W. Simpson, M. B. Lazarus, D. J. Sherman, R. M. Davis, S. Okuda, W. Massefski, N. Ruiz, D. Kahne, The antibiotic novobiocin binds and activates the ATPase that powers lipopolysaccharide transport. *J. Am. Chem. Soc.* **139**, 17221–17224 (2017).
45. M. C. Pismataro, A. Astolfi, M. L. Barreca, M. Pacetti, S. Schenone, T. Bandiera, A. Carbone, S. Massari, Small molecules targeting DNA polymerase theta (POLθ) as promising synthetic lethal agents for precision cancer therapy. *J. Med. Chem.* **66**, 6498–6522 (2023).
46. K. W. Caldecott, C. K. McKeown, J. D. Tucker, S. Ljungquist, L. H. Thompson, An interaction between the mammalian DNA repair protein XRCC1 and DNA ligase III. *Mol. Cell. Biol.* **14**, 68–76 (1994).
47. D. S. Levin, A. E. McKenna, T. A. Motycka, Y. Matsumoto, A. E. Tomkinson, Interaction between PCNA and DNA ligase I is critical for joining of Okazaki fragments and long-patch base-excision repair. *Curr. Biol.* **10**, 919–9S2 (2000).
48. R. S. Tebbs, L. H. Thompson, J. E. Cleaver, Rescue of Xrcc1 knockout mouse embryo lethality by transgene-complementation. *DNA Repair* **2**, 1405–1417 (2003).
49. J. Wang, C. A. Sadeghi, R. L. Frock, DNA-PKcs suppresses illegitimate chromosome rearrangements. *Nucleic Acids Res.* **52**, 5048–5066 (2024).
50. J. T. Meier, S. M. Lewis, P nucleotides in V(D)J recombination: A fine-structure analysis. *Mol. Cell. Biol.* **13**, 1078–1092 (1993).
51. A. L. Bredemeyer, C.-Y. Huang, L. M. Walker, C. H. Bassing, B. P. Sleckman, Aberrant V(D)J recombination in ataxia telangiectasia mutated-deficient lymphocytes is dependent on nonhomologous DNA end joining. *J. Immunol.* **181**, 2620–2625 (2008).
52. J. A. Neal, Y. Xu, M. Abe, E. Hendrickson, K. Meek, Restoration of ATM expression in DNA-PKcs-deficient cells inhibits signal end joining. *J. Immunol.* **196**, 3032–3042 (2016).
53. E. M. Barajas-Mora, E. Kleiman, J. Xu, N. C. Carrico, H. Lu, E. M. Oltz, C. Murre, A. J. Feeney, A B-cell-specific enhancer orchestrates nuclear architecture to generate a diverse antigen receptor repertoire. *Mol. Cell* **73**, 48–60.e5 (2019).
54. L. Hill, G. Wutz, M. Jaritz, H. Tagoh, L. Calderón, J.-M. Peters, A. Goloborodko, M. Busslinger, Igh and Igk loci use different folding principles for V gene recombination due to distinct chromosomal architectures of pro-B and pre-B cells. *Nat. Commun.* **14**, 2316 (2023).
55. S. Zha, C. Guo, C. Boboila, V. Oksenych, H.-L. Cheng, Y. Zhang, D. R. Wesemann, G. Yuen, H. Patel, P. H. Goff, R. L. Dubois, F. W. Alt, ATM damage response and XLF repair factor are functionally redundant in joining DNA breaks. *Nature* **469**, 250–254 (2011).
56. I. Talhaoui, N. A. Lebedeva, G. Zarkovic, C. Saint-Pierre, M. M. Kutuzov, M. V. Sukhanova, B. T. Matkarimov, D. Gasparutto, M. K. Saparbaev, O. I. Lavrik, A. A. Ishchenko, Poly(ADP-ribose) polymerases covalently modify strand break termini in DNA fragments in vitro. *Nucleic Acids Res.* **44**, 9279–9295 (2016).
57. C. Thomas, Y. Ji, C. Wu, H. Datz, C. Boyle, B. MacLeod, S. Patel, M. Ampofo, M. Currie, J. Harbin, K. Pechenkina, N. Lodhi, S. J. Johnson, A. V. Tulin, Hit and run versus long-term activation of PARP-1 by its different domains fine-tunes nuclear processes. *Proc. Natl. Acad. Sci. U.S.A.* **116**, 9941–9946 (2019).
58. S. Kumamoto, A. Nishiyama, Y. Chiba, R. Miyashita, C. Konishi, Y. Azuma, M. Nakanishi, HPF1-dependent PARP activation promotes LIG3-XRCC1-mediated backup pathway of Okazaki fragment ligation. *Nucleic Acids Res.* **49**, 5003–5016 (2021).
59. N. A. W. Bell, J. E. Molloy, Single-molecule force spectroscopy reveals binding and bridging dynamics of PARP1 and PARP2 at DNA double-strand breaks. *Proc. Natl. Acad. Sci. U.S.A.* **120**, e2214209120 (2023).
60. C. Blessing, I. K. Mandemaker, C. Gonzalez-Leal, J. Preisser, A. Schomburg, A. G. Ladurner, The oncogenic helicase ALC1 regulates PARP inhibitor potency by trapping PARP2 at DNA breaks. *Mol. Cell* **80**, 862–875.e6 (2020).
61. M. A. Galindo-Campos, M. Bedora-Faure, J. Farrés, C. Lescale, L. Moreno-Lama, C. Martínez, J. Martín-Caballero, C. Ampurdanés, P. Aparicio, F. Dantzer, A. Cerutti, L. Deriano, J. Yélamos, Coordinated signals from the DNA repair enzymes PARP-1 and PARP-2 promotes B-cell development and function. *Cell Death Differ.* **26**, 2667–2681 (2019).
62. Z. Li, Y. Li, M. Tang, B. Peng, X. Lu, Q. Yang, Q. Zhu, T. Hou, M. Li, C. Liu, L. Wang, X. Xu, Y. Zhao, H. Wang, Y. Yang, W.-G. Zhu, Destabilization of linker histone H1.2 is essential for ATM activation and DNA damage repair. *Cell Res.* **28**, 756–770 (2018).
63. T. Thorslund, A. Ripplinger, S. Hoffmann, T. Wild, M. Uckelmann, B. Villumsen, T. Narita, T. K. Sixma, C. Choudhary, S. Bekker-Jensen, N. Mailand, Histone H1 couples initiation and amplification of ubiquitin signalling after DNA damage. *Nature* **527**, 389–393 (2015).
64. O. Mortusewicz, J.-C. Amé, V. Schreiber, H. Leonhardt, Feedback-regulated poly(ADP-ribosyl)ation by PARP-1 is required for rapid response to DNA damage in living cells. *Nucleic Acids Res.* **35**, 7665–7675 (2007).
65. V. Hurst, K. Challa, K. Shimada, S. M. Gasser, Cytoskeleton integrity influences XRCC1 and PCNA dynamics at DNA damage. *Mol. Biol. Cell* **32**, br6 (2021).
66. J.-F. Haince, D. McDonald, A. Rodrigue, U. Déry, J.-Y. Masson, M. J. Hendzel, G. G. Poirier, PARP1-dependent kinetics of recruitment of MRE11 and NBS1 proteins to multiple DNA damage sites. *J. Biol. Chem.* **283**, 1197–1208 (2008).
67. H. Hanzlikova, W. Gittens, K. Krejcikova, Z. Zeng, K. W. Caldecott, Overlapping roles for PARP1 and PARP2 in the recruitment of endogenous XRCC1 and PNKP into oxidized chromatin. *Nucleic Acids Res.* **45**, 2546–2557 (2017).
68. A. A. Demin, K. Hirota, M. Tsuda, M. Adamowicz, R. Hailstone, J. Brazina, W. Gittens, I. Kalasova, Z. Shao, S. Zha, H. Sasanuma, H. Hanzlikova, S. Takeda, K. W. Caldecott, XRCC1 prevents toxic PARP1 trapping during DNA base excision repair. *Mol. Cell* **81**, 3018–3030. e5 (2021).
69. U. Thapar, B. Demple, Deployment of DNA polymerases beta and lambda in single-nucleotide and multinucleotide pathways of mammalian base excision DNA repair. *DNA Repair* **76**, 11–19 (2019).
70. E. Crespan, T. Czabany, G. Maga, U. Hübscher, Microhomology-mediated DNA strand annealing and elongation by human DNA polymerases λ and β on normal and repetitive DNA sequences. *Nucleic Acids Res.* **40**, 5577–5590 (2012).
71. K. Yamamoto, Y. Wang, W. Jiang, X. Liu, R. L. Dubois, C.-S. Lin, T. Ludwig, C. J. Bakkenist, S. Zha, Kinase-dead ATM protein causes genomic instability and early embryonic lethality in mice. *J. Cell Biol.* **198**, 305–313 (2012).
72. K. Yamamoto, J. Wang, L. Sprinzen, J. Xu, C. J. Haddock, C. Li, B. J. Lee, D. G. Loredan, W. Jiang, A. Vindigni, D. Wang, R. Rabadan, S. Zha, Kinase-dead ATM protein is highly oncogenic and can be preferentially targeted by topo-isomerase I inhibitors. *eLife* **5**, e14709 (2016).
73. S. Difilippantonio, E. Gapud, N. Wong, C.-Y. Huang, G. Mahowald, H. T. Chen, M. J. Kruhlak, E. Callen, F. Livak, M. C. Nussenzweig, B. P. Sleckman, A. Nussenzweig, 53BP1 facilitates long-range DNA end-joining during V(D)J recombination. *Nature* **456**, 529–533 (2008).
74. E. Vincendeau, W. Wei, X. Zhang, C. Planchais, W. Yu, H. Lenden-Hasse, T. Cokelaer, J. Pipoli da Fonseca, H. Mouquet, D. J. Adams, F. W. Alt, S. P. Jackson, G. Balmus, C. Lescale, L. Deriano, SHLD1 is dispensable for 53BP1-dependent V(D)J recombination but critical for productive class switch recombination. *Nat. Commun.* **13**, 3707 (2022).
75. V. Oksenych, F. W. Alt, V. Kumar, B. Schwer, D. R. Wesemann, E. Hansen, H. Patel, A. Su, C. Guo, Functional redundancy between repair factor XLF and damage response mediator 53BP1 in V(D)J recombination and DNA repair. *Proc. Natl. Acad. Sci. U.S.A.* **109**, 2455–2460 (2012).
76. S. Kilic, A. Lezaja, M. Gatti, E. Bianco, J. Michelena, R. Imhof, M. Altmeyer, Phase separation of 53BP1 determines liquid-like behavior of DNA repair compartments. *EMBO J.* **38**, e101379 (2019).
77. C. Gelot, M. T. Kovacs, S. Miron, E. Mylne, A. Haan, L. Boeffard-Dosierre, R. Ghouil, T. Popova, F. Dingli, D. Loew, J. Guirouilh-Barbat, E. Del Nery, S. Zinn-Justin, R. Ceccaldi, Polθ is phosphorylated by PLK1 to repair double-strand breaks in mitosis. *Nature* **621**, 415–422 (2023).
78. A. Brambati, O. Sacco, S. Porcella, J. Heyza, M. Kareh, J. C. Schmidt, A. Sfeir, RHINO directs MMEJ to repair DNA breaks in mitosis. *Science* **381**, 653–660 (2023).
79. A. Orthwein, A. Fradet-Turcotte, S. M. Noordermeer, M. D. Canny, C. M. Brun, J. Strecker, C. Escribano-Diaz, D. Durocher, Mitosis inhibits DNA double-strand break repair to guard against telomere fusions. *Science* **344**, 189–193 (2014).
80. D.-H. Lee, S. S. Acharya, M. Kwon, P. Drane, Y. Guan, G. Adelmant, P. Kalev, J. Shah, D. Pellman, J. A. Marto, D. Chowdhury, Dephosphorylation enables the recruitment of 53BP1 to double-strand DNA breaks. *Mol. Cell* **54**, 512–525 (2014).
81. K. Yata, J.-Y. Bleuyard, R. Nakato, C. Ralf, Y. Katou, R. A. Schwab, W. Niedzwiedz, K. Shirahige, F. Esashi, BRCA2 coordinates the activities of cell-cycle kinases to promote genome stability. *Cell Rep.* **7**, 1547–1559 (2014).
82. W. Feng, D. A. Simpson, J. Carvajal-Garcia, B. A. Price, R. J. Kumar, L. E. Mose, R. D. Wood, N. Rashid, J. E. Purvis, J. S. Parker, D. A. Ramsden, G. P. Gupta, Genetic determinants of cellular addiction to DNA polymerase theta. *Nat. Commun.* **10**, 4286 (2019).
83. S. L. Hewitt, J. B. Wong, J.-H. Lee, M. Nishana, H. Chen, M. Coussens, S. M. Arnal, L. M. Blumenberg, D. B. Roth, T. T. Paull, J. A. Skok, The conserved ATM kinase RAG2-S365 phosphorylation site limits cleavage events in individual cells independent of any repair defect. *Cell Rep.* **21**, 979–993 (2017).
84. K. A. Menear, C. Adcock, R. Boulter, X.-L. Cockcroft, L. Copsey, A. Cranston, K. J. Dillon, J. Drzewiecki, S. Garman, S. Gomez, H. Javaid, F. Kerrigan, C. Knights, A. Lau, V. M. Loh Jr., I. T. W. Matthews, S. Moore, M. J. O'Connor, G. C. M. Smith, N. M. B. Martin, 4-[3-(4-cyclopropanecarbonylpiperazine-1-carbonyl)-4-fluorobenzyl]-2H-phthalazin-1-one: A novel bioavailable inhibitor of poly(ADP-ribose) polymerase-1. *J. Med. Chem.* **51**, 6581–6591 (2008).
85. P. C. Fong, D. S. Boss, T. A. Yap, A. Tutt, P. Wu, M. Mergui-Roelvink, P. Mortimer, H. Swaisland, A. Lau, M. J. O'Connor, A. Ashworth, J. Carmichael, S. B. Kaye, J. H. M. Schellens, J. S. de Bono, Inhibition of poly(ADP-ribose) polymerase in tumors from BRCAMutation carriers. *N. Engl. J. Med.* **361**, 123–134 (2009).
86. J. Murai, S.-Y. N. Huang, A. Renaud, Y. Zhang, J. Ji, S. Takeda, J. Morris, B. Teicher, J. H. Doroshow, Y. Pommier, Stereospecific PARP trapping by BMN 673 and comparison with olaparib and rucaparib. *Mol. Cancer Ther.* **13**, 433–443 (2014).
87. J. K. Litton, H. S. Rugo, J. Ettl, S. A. Hurvitz, A. Gonçalves, K.-H. Lee, L. Fehrenbacher, R. Yerushalmi, L. A. Mina, M. Martin, H. Roché, Y.-H. Im, R. G. W. Quek, D. Markova,

I. C. Tudor, A. L. Hannah, W. Eiermann, J. L. Blum, Talazoparib in patients with advanced breast cancer and a germline BRCA mutation. *N. Engl. J. Med.* **379**, 753–763 (2018).
88. J. Zhou, C. Gelot, C. Pantelidou, A. Li, H. Yücel, R. E. Davis, A. Färkkilä, B. Kochupurakkal, A. Syed, G. I. Shapiro, J. A. Tainer, B. S. J. Blagg, R. Ceccaldi, A. D. D'Andrea, A first-in-class polymerase theta inhibitor selectively targets homologous-recombination-deficient tumors. *Nat. Cancer* **2**, 598–610 (2021).
89. D. Zatreanu, H. M. R. Robinson, O. Alkhatib, M. Boursier, H. Finch, L. Geo, D. Grande, V. Grinkevich, R. A. Heald, S. Langdon, J. Majithiya, C. McWhirter, N. M. B. Martin, S. Moore, J. Neves, E. Rajendra, M. Ranzani, T. Schaedler, M. Stockley, K. Wiggins, R. Brough, S. Sridhar, A. Gulati, N. Shao, L. M. Badder, D. Novo, E. G. Knight, R. Marlow, S. Haider, E. Callen, G. Hewitt, J. Schimmel, R. Prevo, C. Alli, A. Ferdinand, C. Bell, P. Blencowe, C. Bot, M. Calder, M. Charles, J. Curry, T. Ekwuru, K. Ewings, W. Krajewski, E. MacDonald, H. McCarron, L. Pang, C. Pedder, L. Rigoreau, M. Swarbrick, E. Wheatley, S. Willis, A. C. Wong, A. Nussenzweig, M. Tijsterman, A. Tutt, S. J. Boulton, G. S. Higgins, S. J. Pettitt, G. C. M. Smith, C. J. Lord, Polθ inhibitors elicit BRCA-gene synthetic lethality and target PARP inhibitor resistance. *Nat. Commun.* **12**, 3636 (2021).
90. R. Abdel-Samad, P. Aouad, H. Gali-Muhtasib, Z. Sweidan, R. Hmadi, H. Kadara, E. L. D'Andrea, A. Fucci, C. Pisano, N. Darwiche, Mechanism of action of the atypical retinoid ST1926 in colorectal cancer: DNA damage and DNA polymerase α. *Am. J. Cancer Res.* **8**, 39–55 (2018).
91. T. Han, M. Goralski, E. Capota, S. B. Padrick, J. Kim, Y. Xie, D. Nijhawan, The antitumor toxin CD437 is a direct inhibitor of DNA polymerase α. *Nat. Chem. Biol.* **12**, 511–515 (2016).
92. K. M. Foote, J. W. M. Nissink, T. McGuire, P. Turner, S. Guichard, J. W. T. Yates, A. Lau, K. Blades, D. Heathcote, R. Odedra, G. Wilkinson, Z. Wilson, C. M. Wood, P. J. Jewsbury, Discovery and characterization of AZD6738, a potent inhibitor of ataxia telangiectasia mutated and Rad3 related (ATR) kinase with application as an anticancer agent. *J. Med. Chem.* **61**, 9889–9907 (2018).
93. S. E. Golding, E. Rosenberg, N. Valerie, I. Hussaini, M. Frigerio, X. F. Cockcroft, W. Y. Chong, M. Hummersone, L. Rigoreau, K. A. Menear, M. J. O'Connor, L. F. Povirk, T. van Meter, K. Valerie, Improved ATM kinase inhibitor KU-60019 radiosensitizes glioma cells, compromises insulin, AKT and ERK prosurvival signaling, and inhibits migration and invasion. *Mol. Cancer Ther.* **8**, 2894–2902 (2009).
94. W. Liu, M. Zhou, Z. Li, H. Li, P. Polaczek, H. Dai, Q. Wu, C. Liu, K. K. Karanja, V. Popuri, S.-O. Shan, K. Schlacher, L. Zheng, J. L. Campbell, B. Shen, A selective small molecule DNA2 inhibitor for sensitization of human cancer cells to chemotherapy. *EBioMedicine* **6**, 73–86 (2016).
95. A. Shibata, D. Moiani, A. S. Arvai, J. Perry, S. M. Harding, M.-M. Genois, R. Maity, S. van Rossum-Fikkert, A. Kertokalio, F. Romoli, A. Ismail, E. Ismalaj, E. Petricci, M. J. Neale, R. G. Bristow, J.-Y. Masson, C. Wyman, P. A. Jeggo, J. A. Tainer, DNA double-strand break repair pathway choice is directed by distinct MRE11 nuclease activities. *Mol. Cell* **53**, 7–18 (2014).
96. L. Zhao, R. L. Frock, Z. Du, J. Hu, L. Chen, M. S. Krangel, F. W. Alt, Orientation-specific RAG activity in chromosomal loop domains contributes to Tcrd V(D)J recombination during T cell development. *J. Exp. Med.* **213**, 1921–1936 (2016).

Acknowledgments: We thank J. Tainer for the Mre11 inhibitors (PFM01, PFM03, and PFM39) and the Stanford Cancer Institute core facilities. Figs. 2A and 6A and figs. S3B, S4B, S5A, S6A, S7A, and S17A were generated from the Integrative Genomics Viewer (igv.org). **Funding:** This research was supported in part by the V Scholar Grant (2019-003) from the V Foundation for Cancer Research (R.L.F.) and the Research Scholar Grant (RSG-23-1038994-01DMC) from the American Cancer Society (R.L.F.). **Author contributions:** Conceptualization: J.W. and R.L.F. Methodology: J.W. and R.L.F. Investigation: J.W., C.A.S., L.V.L., and M.L.B. Software: J.W. and M.L.B. Visualization: J.W. and R.L.F. Formal analysis: J.W., M.L.B., and R.L.F. Validation: J.W. and R.L.F. Data curation: J.W. Funding acquisition: R.L.F. Supervision: J.W. and R.L.F. Writing—original draft: J.W. and R.L.F. Writing—review and editing: J.W., C.A.S., L.V.L., M.L.B., and R.L.F. **Competing interests:** R.L.F. is an inventor of HTGTS (patent #10640820; 2 May 2020) held by Children's Medical Center. All other authors declare that they have no competing interests. **Data and materials availability:** All data needed to evaluate the conclusions in the paper are present in the paper and/or the Supplementary Materials. Genome-wide junction maps and related sequencing data are on GEO under the ascension numbers GSE242952, GSE246239, and GSE263165. Scripts used for analysis are available on Zenodo at https://doi.org/10.5281/zenodo.11099892.

Submitted 12 December 2023
Accepted 11 June 2024
Published 31 July 2024
10.1126/sciadv.adn4682